PLANETARY SCIENCE

Alteration history of Séítah formation rocks inferred by PIXL x-ray fluorescence, x-ray diffraction, and multispectral imaging on Mars

Michael M. Tice[1]*, Joel A. Hurowitz[2], Abigail C. Allwood[3], Michael W. M. Jones[4], Brendan J. Orenstein[5], Scott Davidoff[3], Austin P. Wright[6], David A.K. Pedersen[7], Jesper Henneke[7], Nicholas J. Tosca[8], Kelsey R. Moore[9], Benton C. Clark[10], Scott M. McLennan[2], David T. Flannery[5], Andrew Steele[11], Adrian J. Brown[12], Maria-Paz Zorzano[13], Keyron Hickman-Lewis[14], Yang Liu[3], Scott J. VanBommel[15], Mariek E. Schmidt[16], Tanya V. Kizovski[16], Allan H. Treiman[17], Lauren O'Neil[18], Alberto G. Fairén[19,20], David L. Shuster[21], Sanjeev Gupta[22], The PIXL Team

Collocated crystal sizes and mineral identities are critical for interpreting textural relationships in rocks and testing geological hypotheses, but it has been previously impossible to unambiguously constrain these properties using in situ instruments on Mars rovers. Here, we demonstrate that diffracted and fluoresced x-rays detected by the PIXL instrument (an x-ray fluorescence microscope on the Perseverance rover) provide information about the presence or absence of coherent crystalline domains in various minerals. X-ray analysis and multispectral imaging of rocks from the Séítah formation on the floor of Jezero crater shows that they were emplaced as coarsely crystalline igneous phases. Olivine grains were then partially dissolved and filled by finely crystalline or amorphous secondary silicate, carbonate, sulfate, and chloride/oxychlorine minerals. These results support the hypothesis that Séítah formation rocks represent olivine cumulates altered by fluids far from chemical equilibrium at low water-rock ratios.

INTRODUCTION

It has been known since the Mariner 9 orbiter and Viking missions that liquid water was an important geological agent early in the history of Mars [e.g., (*1*)]; however, one of the great accomplishments of Mars exploration over the past two decades has been the recognition of remarkably diverse aqueous processes in shaping the planet's near-surface mineralogy, chemistry and geology. Spectroscopic observations from orbit revealed an array of near-surface secondary minerals [e.g., (*2*, *3*)], including Ca-Mg-Fe-sulfates, carbonates, chlorides, di-tri-octahedral clays, amorphous silica, oxide-hydroxides, and most of these phases (plus additional ones) have been confirmed through in situ examination by a variety of instruments on rovers and landers [e.g., (*3*–*6*)]. In turn, the geological context of these secondary minerals has been used to constrain a variety of aqueous and sedimentary processes [e.g., (*7*)], including depositional processes (e.g., evaporites, diagenetic cements, and fracture fills) and alteration processes (e.g., chemical weathering, groundwater diagenesis, and epithermal through hydrothermal alteration). Although the past actions of these processes have been identified and broadly characterized on Mars, many of the key questions associated with more in-depth interpretations, such as fluid/rock ratios, fluid chemistry, fluid pathways, and mineral reactions, remain outstanding. To a substantial degree, this is because it is not possible to develop the required paragenetic sequences (order and chemical context in which secondary minerals formed) and detailed chemistry of the alteration phases without understanding the relationships between microtextures and mineralogy/chemistry.

An accurate reconstruction of the geological history of any rock requires detailed petrographic characterization, including analytical techniques that coregister chemistry, mineralogy, and texture at spatial scales comparable to the features or processes under investigation. For rocks with millimeter-scale grains, examination of formation and alteration processes thus requires investigation at the submillimeter scale. On Earth, this is commonly accomplished with combinations of several field and laboratory tools, including hand-lenses, petrographic microscopes, and electron microscopes and microprobes. These analyses provide critical constraints when combined with observations at larger scales for testing geologic hypotheses.

In contrast, except for laboratory analyses performed on martian meteorites, it has been difficult to apply similar techniques to address geologic questions on Mars. This is because previous rover missions

[1]Department of Geology and Geophysics, Texas A&M University, College Station, TX 77843, USA. [2]Department of Geosciences, Stony Brook University, Stony Brook, NY 11794-2100, USA. [3]Jet Propulsion Laboratory, California Institute of Technology, Pasadena, CA 91109, USA. [4]School of Chemistry and Physics and Central Analytical Research Facility, Queensland University of Technology, Brisbane, QLD 4000, Australia. [5]School of Earth and Atmospheric Sciences, Queensland University of Technology, Brisbane, QLD 4000, Australia. [6]School of Computational Science and Engineering, Georgia Institute of Technology, Atlanta, GA 30332, USA. [7]Technical University of Denmark, DTU Space, Department of Measurement and Instrumentation, Kongbens Lyngby, 2800, Denmark. [8]Department of Earth Sciences, University of Cambridge, Cambridge CB2 3EQ, UK. [9]Division of Geological and Planetary Sciences, California Institute of Technology, Pasadena, CA 91125, USA. [10]Space Science Institute, Boulder, CO 80301, USA. [11]Earth and Planetary Laboratory, Carnegie Institution for Science, Washington, DC 20015, USA. [12]Plancius Research, Severna Park, MD 21146, USA. [13]Centro de Astrobiologia, Instituto National de Tecnica Aerospacial, Madrid, Spain. [14]Department of Earth Sciences, Natural History Museum, London SW7 5BD, UK. [15]McDonnell Center for the Space Sciences, Department of Earth and Planetary Sciences, Washington University of St. Louis, St. Louis, MO 63130, USA. [16]Department of Earth Sciences, Brock University, St. Catharines, ON L2S 3A1, Canada. [17]Lunar and Planetary Institute (USRA), Houston, TX 77058, USA. [18]Department of Earth and Space Sciences, University of Washington, Seattle, WA 98052, USA. [19]Centro de Astrobiología (CSIC-INTA), Torrejón de Ardoz, Madrid, Spain. [20]Department of Astronomy, Cornell University, Ithaca, NY 14850, USA. [21]Department of Earth and Planetary Science, University of California, Berkeley, CA 94720, USA. [22]Department of Earth Science and Engineering, Imperial College London, London SW7 2AZ, UK.
*Corresponding author. Email: mtice@geos.tamu.edu

on Mars did not have instruments well suited for petrographic analyses available for in situ investigations. As a result, rover-based investigations have had to rely on serendipitous natural experiments and/or have had to go to great lengths to tie chemistry and texture together to solve important questions related to mineralogy, chemistry, and habitability [e.g., (*8*–*10*)]. Unfortunately, these approaches are not always possible, resulting in significant ambiguity in deciphering the processes responsible for observed textural fabrics. The PIXL instrument [Planetary Instrument for X-ray Lithochemistry; (*11*)] on the Mars 2020 Perseverance rover payload provides this capability. PIXL capabilities include coaligned imaging and x-ray fluorescence (XRF), as well as multispectral imaging and x-ray diffraction, at spatial scales ranging from ~50 μm (PIXL image resolution) to ~120 μm (PIXL x-ray spot size) over areas up to ~6.25 cm^2 in size (comparable to a standard petrographic thin section, ~12.5 cm^2).

Jezero crater and the Séítah formation

Jezero crater, the landing site of the Mars 2020 Perseverance rover, is a 45-km-diameter impact crater, thought to have formed ~3.9 billion years ago, near the western edge of Isidis Planitia [e.g., (*12*, *13*)]. A large delta sits just inside the western crater rim (*14*, *15*), at the terminus of a fluvial channel that drained hinterlands located west of Jezero (*13*). The delta and an outflow channel suggest that there was once a lake, a habitable paleoenvironment, with depositional processes that would have provided taphonomic opportunities for preserving signs of life, if any existed there.

A number of generally flat-lying rock units that have been mapped from orbit (*16*) surround the delta at the crater floor. These floor units include the light-toned, polygonally fractured, pyroxene-bearing Máaz formation and the light-toned, ridge-forming, layered olivine and carbonate-bearing Séítah formation (*17*). Regions with similar olivine/carbonate mineralogy extend far beyond the rim of Jezero crater, across the Northeast Syrtis (*18*), Nili Fossae (*19*), and Libya Montes regions (*12*, *20*), with an estimated total outcrop exposure of >70,000 km^2 (*21*). Several hypotheses for the origin of the olivine unit have been developed using data from orbital instruments. They include impact melt or igneous intrusive complexes (*22*), basaltic flows (*12*, *23*), volcanic ash deposits (*12*, *21*), or clastic material (*24*). Results from the Perseverance payload, including in situ PIXL examination of an outcrop of the Séítah formation, indicate that at least part of this unit formed as an olivine cumulate, either as a thick ponded lava flow, a shallow intrusive body, or a thick impact melt sheet (*25*, *26*).

Estimated compositions for carbonate minerals in regional olivine- and carbonate-bearing lithologies range from pure Mg-endmember magnesite and hydromagnesite to more ferroan compositions (*27*–*31*). Competing hypotheses for the origin of the carbonate include surface weathering reactions, soil-forming processes, and/or serpentinization reactions (*27*–*31*). Each hypothesis has specific predictions of textural features expected for different carbonate-forming environments [see discussion in (*29*) and references therein]. For example, carbonate minerals commonly occur in serpentinized rocks as late-stage precipitates filling fractures and voids after serpentine-group silicate minerals completely or partially replace olivine and pyroxene. This carbonate is commonly either microcrystalline (crystal domains, <50 μm) or coarsely crystalline (domains up to several millimeters in diameter). In contrast, the carbonation of olivine-bearing rocks by chemical weathering processes driven by low/ambient temperature meteoric water or groundwater tends to produce microcrystalline carbonate minerals that partially dissect or replace olivine grains and are commonly associated with low-Fe, amorphous, silicate minerals. Last, soil formation, understood broadly as a combination of chemical weathering and localized chemical redistribution, commonly produces carbonate mineral nodules with varying crystallinity that reflects different levels of mineral saturation in precipitating fluids. Here, we use PIXL observations of chemical, mineral, and textural associations between olivine grains, carbonate minerals, and other secondary minerals, together with their inferred crystallinities, to distinguish between these formation hypotheses proposed for secondary minerals in the Séítah formation and—by extrapolation—the regional olivine-carbonate unit to which it has been compositionally associated.

In situ abrasion patch investigation of the Séítah formation

The Séítah formation is composed of two members: the strongly layered Bastide member and the overlying cavity-rich, structureless Content member (*17*). Most layers of the Bastide member are 1 to 3 cm thick, with the thickest layers reaching up to 40 cm. Natural surfaces of Bastide member outcrops are composed of grain-supported 2- to 3-mm-diameter dark gray or green crystals with lighter-toned, frequently brown material between and sometimes rimming grains. A few submillimeter-scale bright white patches are also present.

An abraded patch with the target name "Dourbes" on the "Brac" outcrop in the Séítah formation was prepared using the Perseverance rover's abrasion drill bit (*32*). PIXL collected reflected light images of Dourbes at a standoff distance of 41 mm and performed two XRF scans on Dourbes at a distance of 25.5 mm. At the 41-mm standoff, the field of view of the micro-context camera (MCC) is ~46 mm by ~39 mm with a resolution of ~65 μm/pixel. The XRF scans are composed of two adjacent maps, in which the PIXL x-ray beam was rastered across areas of 4.0 mm by 12.5 mm and 5.0 mm by 7.0 mm with a step size of 120 μm between spots. An energy-dispersive XRF spectrum was collected at each spot using a dwell of 10 s per spot. Additional details about the scan data collection process can be found in (*25*).

RESULTS

Mineral identification

Mineral endmember compositions were identified by comparison to ideal stoichiometric compositions using combinations of molar ternary diagrams (Figs. 1 and 2). In particular, consistent with other analyses (*25*, *33*), we have identified olivine (Fo_{55}), augite pyroxene, feldspathic mesostasis (Fig. 1), various Fe,Cr,Ti-spinels, and merrillite.

A silicate phase was identified as a distinct endmember with molar $0.4 < (FeO + MgO)/SiO_2 < 1$, $Mg/(Mg + Fe) \approx 0.55$, and low Al_2O_3. We call this phase "low-(Fe,Mg)-silicate" owing to its relatively silica-rich nature (Fig. 1). Because the low-(Fe,Mg)-silicate is not present in areas that are larger than the PIXL analytical spot size, it is not known whether this material has a well-defined composition, only observed here in physical mixtures with other phases, or whether it represents a range of compositions and is not a true mineral.

An (Fe,Mg)-carbonate was tentatively identified as a low-SiO_2, low-Al_2O_3, and low-SO_3 phase with FeO, MgO, and CaO as the primary observed oxides (Fig. 1). The relative abundances of FeO, MgO, and CaO (45:49:6 mole percent) in this endmember are consistent

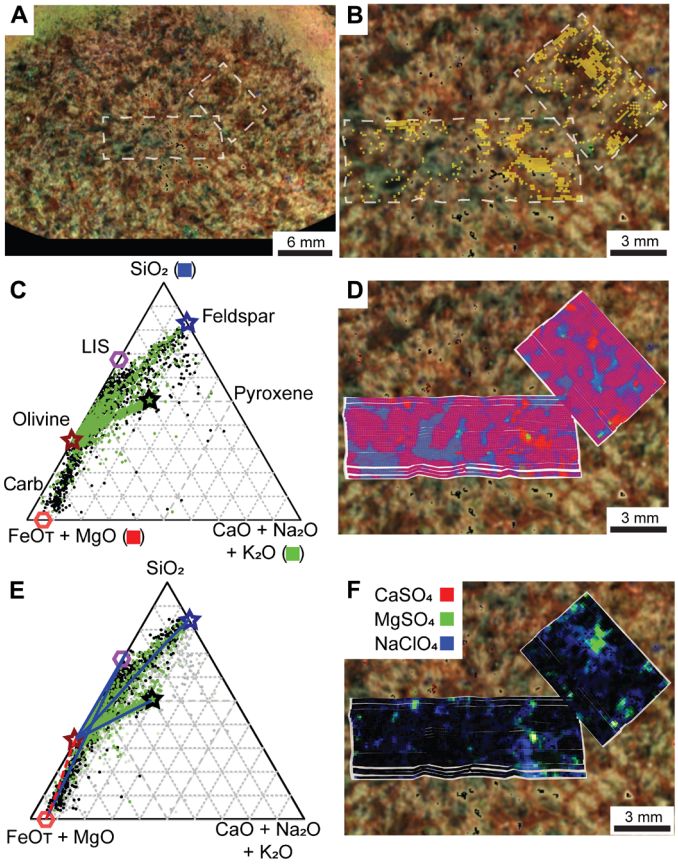

Fig. 1. Minerals and crystallinity. (**A**) Reconstructed color stack with red = 735 nm [near infrared (NIR)], green (G) = 530 nm, and blue (B) = 450 nm. Note the abundant tan millimeter-scale grains with dark brown and green patches. PIXL x-ray map areas (B, D, and F) are indicated with dashed white boxes. (**B**) Areas with no detected diffraction overlaid with slightly transparent yellow. Nondiffracting materials both line visible grain boundaries and cut into grains. (**C**) Mineral classification ternary diagram using molar abundances, with identified primary (stars) and secondary (hexagons) mineral endmembers indicated. Diffracting spots in green. Nondiffracting spots in black. Carb, (Fe,Mg)-carbonate; LIS, low-(Fe,Mg) silicate. Red, green, and blue channels in (D) indicated next to each pole. (**D**) False color map of PIXL measurement patches indicating the presence of various minerals. Coloration derived from ternary diagram in (C), with each color channel intensity reflecting closeness to one of the poles: red, FeO-T + MgO; green, $CaO + Na_2O + K_2O$; and blue, SiO_2. (**E**) Mineral classification ternary diagram as in (C) but with simple accessory minerals (merrillite, calcium sulfate, magnesium sulfate, and Fe,Cr,Ti-spinels) subtracted to aid in the identification of more common minerals. For comparison, presubtraction spots are shown in gray. Blue lines show modeled mixing relationships resulting from partial overlap between minerals under the PIXL measurement spot. Dashed red line shows mixing relationship that should result from grain contacts between olivine and (Fe,Mg)-carbonate, which is not observed. (**F**) False color map of PIXL measurement patches showing distribution of saline minerals. Red, $CaSO_4$; green, $MgSO_4$; and blue, $NaClO_4$. Where both sulfate minerals occur together, the combined color is yellow. Sulfate minerals occur in the centers of patches containing other secondary minerals. Perchlorate lines some olivine grains and partially dissects others.

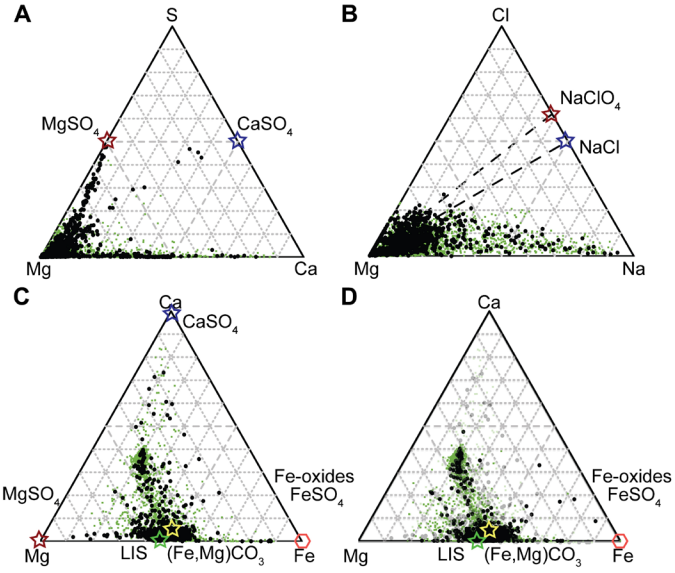

Fig. 2. Mineral endmembers. In each panel, black spots show no diffraction and green spots show diffraction. Molar abundances in all panels. (**A**) Sulfate identification. High-SO_3 regions are classified as $MgSO_4$ or $CaSO_4$. $CaSO_4$ endmember may incorporate some $FeSO_4$. (**B**) Cl-bearing endmember classification. Mixing area results from physical mixing of high-Cl phases with variable amounts of high-Na phase (feldspar). For low-Na abundances, Na correlates with Cl with Na/Cl consistent with the PIXL detection of perchlorate. (**C**) Various endmembers including sulfate minerals, low-(Fe,Mg)-silicate, and (Fe,Mg)-carbonate. (**D**) Same classification diagram as in (C) but with contributions from sulfate minerals and Fe,Cr,Ti-spinels subtracted from each spot. Unsubtracted data are shown in light gray. Removal of accessory minerals and stability of inferred secondary endmembers are shown by tightening of spots around the remaining endmembers.

with compositions of naturally occurring solid solutions of magnesite and siderite (*34*). Notably, Fe/Mg ratios overlap substantially between measurement spots on olivine, low-(Fe,Mg)-silicate, and (Fe,Mg)-carbonate (Fig. 2). In addition, Mg-sulfate and Ca-sulfate phases were identified by MgO/SO_3 and CaO/SO_3 ratios that approached 1 at high SO_3 abundances, respectively (Fig. 2). A Cl-bearing phase is inferred to be a form of NaCl, a Na-oxychlorine species, or both based on these and related measurements by PIXL, when analyzing spots with low concentrations of feldspar-related Na_2O (Fig. 2).

PIXL cannot directly detect elements with atomic numbers less than that of Na ["low-Z elements" (LZEs)] by XRF. Because standard chemical analyses assume that elements are present as oxides, LZE can be inferred from total oxide abundances (i.e., analytical totals), provided that concentration data are not required to be normalized to 100% during quantification [cf. (*10*)]. PIXL oxide quantification does not require normalization (*11*, *25*), so low analytical totals may reflect undetected low mass elements (e.g., H, F, and C), underestimation of some reported elemental abundances because of x-ray absorption by LZE, or both. To test the hypothesis that carbonate minerals are present in the Dourbes scan areas and to check for the presence of water of hydration, we, therefore, examined analytical totals for regions with inferred carbonate and sulfate minerals.

Within all but one of these regions, there is sufficient MgO and FeO to account for the unobserved LZE component if one or both are bound to CO_2 (Fig. 3). We interpret this LZE component as indicating the presence of carbonate minerals or their hydrated forms. The regions in which we infer the presence of carbonate minerals correspond to direct detections of carbonate in colocated Raman

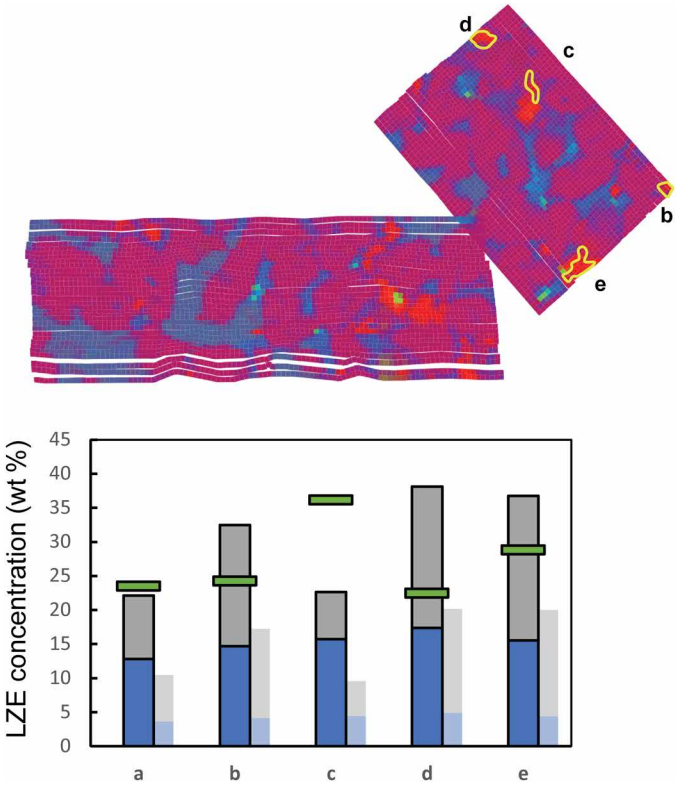

Fig. 3. Carbonate in patches enriched in LZE. Potential concentrations of CO_2 for measurements with high LZE, for (a) dispersed spots and (b, d, and e) four patches partially replacing olivine. Patch (c) fills void space defined by dissected olivine grain boundaries. Predicted LZE levels are if all MgO (blue) and FeO (gray) are bound in carbonate minerals compared to the measured LZE level at those locations (green bars). For comparison, faded bars show mass of LZE as hydrated mineral forms of MgO (brucite) and FeO (hisingerite). Compositions are well explained as combinations of (Fe,Mg)-carbonate and olivine or low-(Fe,Mg)-silicate, neither of which contribute CO_2. The exception is patch (c), which likely contains undetected H_2O from polyhydrated $MgSO_4$. Compositional map as in Fig. 1. wt %, weight %.

spectroscopic measurements by the SHERLOC instrument (*35*). Moreover, the SuperCam instrument has also identified Mg/Fe-carbonates in the Séítah formation (*33*), providing further confidence in our identification. In the region where carbonate minerals are insufficient to account for low analytical totals, $MgSO_4$ is especially abundant. In this case, some hydration of $MgSO_4$ is also likely required. There, the abundance of LZE indicates the possibility of $MgSO_4{\cdot}4H_2O$, a phase consistent with simulations of hydration states for this salt under martian conditions (*36*).

The detection of perchlorate by SHERLOC (*35*) and by SuperCam (*33*) in overlying Máaz formation rocks containing more Cl than Dourbes (Séítah formation) but with similar saline mineral assemblages suggests that some of the Na- and Cl-bearing phase observed by PIXL could be $NaClO_4$. Because perchlorate adds a large oxygen content relative to Cl alone, the XRF matrix effect is significantly different from that of NaCl. The extra oxygen would attenuate Na K_α x-rays more than Cl K_α x-rays, which would lead to a reduction in the apparent Na/Cl ratio relative to the standard laboratory calibration of these two elements. We find that this low ratio is consistent with observed abundances when igneous mineral sources of Na_2O are less abundant (Fig. 2), implying that perchlorate may be present. However, the low abundances of Cl relative to other sources of Na_2O make it difficult to uniquely identify Cl-bearing species, and we do not exclude the possibility of more than one Cl species being present, including chloride (halite) and other oxychlorines, such as chlorates. For simplicity, we will refer to Cl components of Dourbes as perchlorates.

Mixing relationships and mineral contacts

As the PIXL instrument moved over the surface of the abrasion patch, many measurement spots overlapped more than one mineral, producing apparent mixing relationships between mineral endmembers. In addition, physical mixtures of grains smaller than the PIXL spot size produce similar mixing relationships. These mixing relationships thus provide information about grains smaller than 120 μm and mineral contacts and textural relationships potentially resulting from paragenetic relationships.

The physical distributions of saline minerals (sulfates and perchlorates) were mapped by sequentially assigning CaO, MgO, and Na_2O to merrillite, sulfate, and perchlorate, subtracting available oxides with each step ("mineral stripping"). Resulting maps that show the locations of x-ray spectra where these phases were most abundant indicate concentrated regions of $MgSO_4$ with minor $CaSO_4$ at or near the centers of patches containing alteration minerals (Fig. 1F). Perchlorate is distributed throughout alteration patches and commonly penetrates olivine grains.

The distributions of (Fe,Mg)-carbonate and low-(Fe,Mg)-silicate are mappable as regions of low- and high-SiO_2 abundances, respectively (Fig. 1D). Low-(Fe,Mg)-silicate lines patches of alteration minerals and partially replaces olivine grains. (Fe,Mg)-carbonate fills alteration patch centers and may completely replace small olivine grains.

Modeled mixing relationships reflecting different effective measurement spot sizes for major oxides show that mixtures containing olivine as an endmember have feldspar, pyroxene, and low-(Fe,Mg)-silicate as the other endmembers (Fig. 1E). These mixtures reflect locations where olivine and these other phases are in physical contact with one another, with the contact sampled by the PIXL x-ray beam. In contrast, olivine contacts with (Fe,Mg)-carbonate are rare to absent. Of feldspar, pyroxene, olivine, and low-(Fe,Mg)-silicate, (Fe,Mg)-carbonate only contacts low-(Fe,Mg)-silicate. These relationships produce a characteristic paragenetic sequence of low-(Fe,Mg)-silicate replacing or lining olivine, which is followed by infilling (Fe,Mg)-carbonate, which is itself infilled by sulfate minerals (Fig. 4). Perchlorate intermixes with all these phases and further penetrates and dissects olivine (Fig. 4).

Fe-oxides such as hematite and magnetite (Fe_2O_3 and Fe_3O_4, respectively) are unlikely to constitute more than 5 to 10% of the area of any individual analytical spot. In particular, admixture of these minerals with any of the inferred minerals would produce mixing lines toward a more Fe-rich composition (the lower-left pole in Fig. 1C). Instead, once FeO associated with primary igneous Fe-Cr-Ti spinels (*25*) is subtracted from each measurement spot (Fig. 1E), no mixing relationships require a purely Fe-rich endmember.

Crystallinity analysis

While designed primarily as an XRF instrument, PIXL also collects diffraction peaks in its two energy-dispersive detectors, enabling energy-dispersive x-ray diffraction (EDXRD) data to be collected

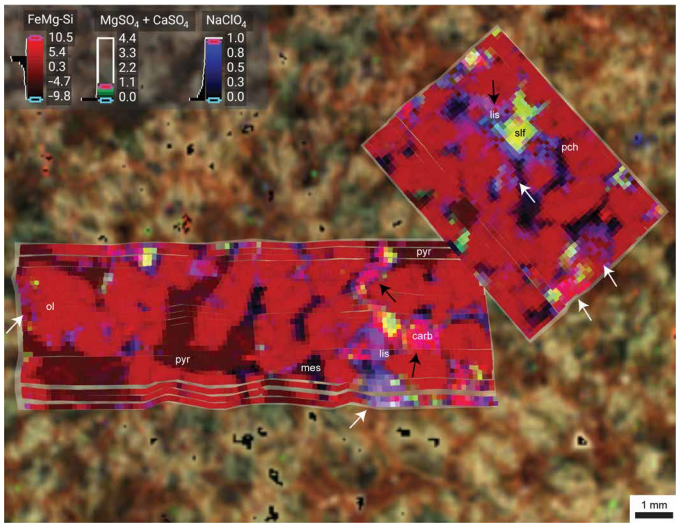

Fig. 4. Secondary mineral associations. False color image of PIXL measurement patches showing associations between secondary minerals [low-(Fe,Mg)-silicate (lis), dull blue-purple; (Fe,Mg)-carbonate (carb), bright red-purple; sulfate minerals (slf), yellow; and $NaClO_4$ (pch), blue] with primary igneous minerals [olivine (ol), red; pyroxene (pyr), dark dull red; mesostasis (mes), black]. Note the partial replacement of olivine by alteration minerals (white arrows) and infilling of dissected olivine grain boundaries by low-(Fe,Mg)-silicate → (Fe,Mg)-carbonate → (Fe,Mg)-carbonate + sulfate minerals (black arrows). Perchlorate is present throughout the alteration assemblage. Color mapping: red, $FeO_T + MgO - SiO_2$; green, $MgSO_4 + CaSO_4$; and blue, $NaClO_4$. Abundances in millimole per gram of rock, with distributions and color mapping indicated in key. Mineral abundances estimated by mineral stripping.

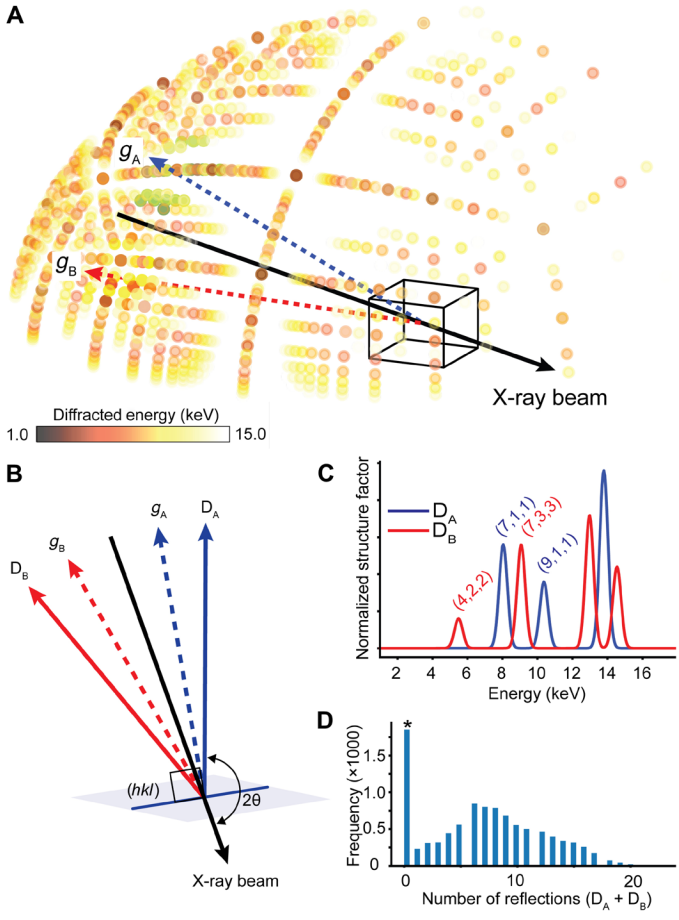

Fig. 5. Likelihood of observing diffraction from a randomly oriented grain. Diffraction detected by the PIXL instrument is analogous to a dual detector EDXRD instrument operating in the back reflection geometry. When the broadband x-ray beam is incident on a crystalline sample, many diffraction planes satisfy the Bragg condition. The direction of the vector normal to the diffraction planes (*g*), together with the energy that satisfies the Bragg condition for energies from 1 to 15 keV, is shown in (**A**), with the point where the vector intersects a sphere depicted as a circle colored according to its energy. Here, the anisotropic nature of diffraction recorded by PIXL is evident. The vectors g_A and g_B correspond to the diffraction planes (*g*) that will be recorded in detectors D_A and D_B, respectively, where (**B**) shows the relationship between the vectors g_A and g_B and the detectors D_A and D_B. An (*hkl*) plane diffracting to detector D_B is shown. Panel (**C**) shows the simulated diffraction recorded by PIXL's detectors for the orientation shown in (A), using the normalized structure factor as a proxy for diffraction intensity, clearly showing different diffraction peaks in each detector. Panel (**D**) shows the number of reflections recorded in both detectors from 10,000 random x-ray beam-crystal orientations. The (*) indicates no reflections recorded ($n = 1851$), giving a probability of detecting diffraction from a randomly orientated crystalline grain of 80.5%.

and interrogated (Fig. 5, A to C) (*25*, *37*–*39*). Modeling the probability of PIXL detecting diffraction in either of its two detectors (Fig. 5D) and experimental data of grain size fractions (fig. S2) show that diffraction peaks are detected with high probability (>80%) and can be readily identified in PIXL spectra for crystal grain sizes of greater than 45 μm. We observe similar crystal size dependence along olivine-pyroxene grain contacts on Mars: Pyroxene diffraction peaks are detected if the x-ray beam overlaps a pyroxene grain by more than 20 to 30 μm (fig. S2). Diffraction peaks can therefore be separated into three classes; (i) diffraction that persists over several neighboring pixels signifying a single crystalline domain greater than the PIXL spot size (*25*, *39*), (ii) diffraction that is isolated to a single pixel signifying one or several domains similar to the PIXL spot size, and, lastly, (iii) the absence of diffraction in a spectrum suggesting an amorphous or microcrystalline (i.e., <40 to 50 μm) material.

We used a trained machine learning classification algorithm to automatically test for the presence of diffraction peaks in all Dourbes spectra. Diffraction peaks are identified in all primary igneous materials (olivine, pyroxene, feldspar, phosphates, and oxides) in the Dourbes scan areas, and thus we conclude that they are crystalline. About 16% of all PIXL scan spots in Dourbes display no diffraction peaks in the energy-dispersive x-ray spectrum from either detector. Thus, we conclude that spots with no diffraction peaks comprise either amorphous phases or minerals with crystalline domain sizes <40 to 50 μm. This amorphous/microcrystalline material is located primarily in dissected olivine grain boundaries and linings rich in low-(Fe,Mg)-silicate and carbonate, sulfate, and perchlorate minerals.

Pyroxene and olivine domain clustering analysis

Clustering of diffraction peaks in pyroxene reveals four distinct groupings of relative orientations between pyroxene domains and the PIXL instrument (Fig. 6A). Notably, three apparently separate regions cluster as a single orientation (<8° relative rotation), consistent with identification of these regions as a single poikilitic grain that crystallized in place in the interstices between cumulate olivine grains (*25*).

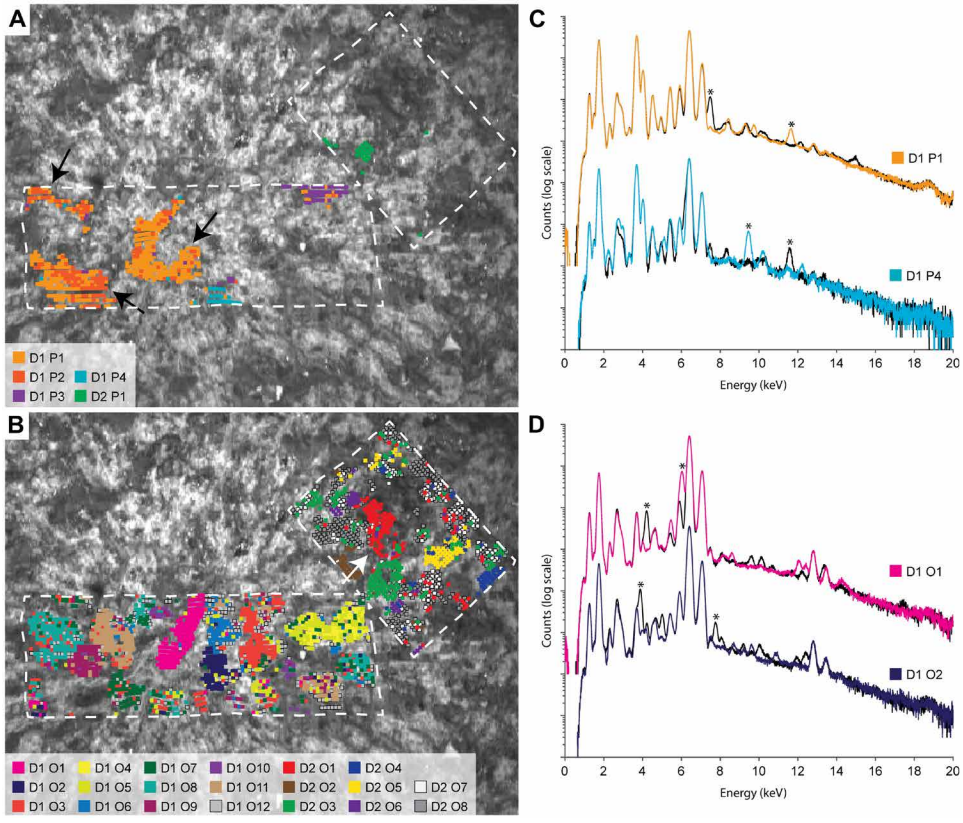

Fig. 6. Pyroxene and olivine grain identification. Individual grains of pyroxene (**A**) and olivine (**B**) are represented by individual colors according to the key in each panel. Grains of the same mineral with small intergrain rotations (D1 P1, D1 P2, and D1 O4, D1 O5) are displayed in similar colors, while clusters that represent no distinct clear cluster (D1 O12, D2 O7, and D2 08) are presented in shades of gray (fig. S2). Note the single poikilitic pyroxene grain intergrown three-dimensionally between olivine grains (black arrows, A) and partially dissected monocrystalline olivine grain (white arrow, B). Spectra from four individual pyroxene and olivine grains from (A) and (B) are shown in (**C**) and (**D**), respectively. The colored and black spectra correspond to detector A and B, respectively, as depicted in Fig. 5. Asterisks in (C) and (D) identify intense diffraction peaks in the spectra and correspond to asterisks in the corresponding panels in fig. S2.

In contrast, olivine diffraction peak clusters show organization as about 20 coarsely monocrystalline grains (Fig. 6B). Domain clustering also shows what appear to be small neighboring olivine grains separated by secondary minerals. These grains share common crystallographic orientations. We interpret this to indicate that these small grains were once larger monocrystalline grains that were partially dissected and replaced.

Comparison with multispectral images

For the Dourbes abrasion patch, multispectral images were collected with PIXL's MCC at a slightly higher standoff distance than nominal, resulting in a ~25% larger area than normal and reduced resolution. However, the resulting images extend mineral and textural interpretations from the PIXL x-ray–based analyses to the larger context of the entire abrasion patch (*25*). Future comparisons with Mastcam-Z, the mast-mounted multispectral camera on Perseverance, will allow similar extension of results to even broader contexts for other abrasion patches. Color ratio images reveal the underlying crystal shape and distribution (Figs. 7 and 8). Specifically, band ratios including the near-infrared (NIR) channel separate the surface into three main regions of pyroxene, olivine plus mesostasis, and secondary minerals plus a small amount of mesostasis.

On the basis of these band ratio histograms, we determined the modal abundance of the three main regions containing pyroxene, olivine plus mesostasis, and secondary minerals, with resulting area coverage estimates of 11.7%, 45.8 to 72.5%, and 15.8 to 42.6%, respectively. This analysis indicates that brown-colored patches with low ratios of green (G), blue (B), and ultraviolet (UV) to NIR comprise large fractions of abrasion patch surfaces. The color reflectance properties do not discriminate well between regions with olivine and mesostasis and regions with altered areas, accounting for some of the apparent high abundance of the secondary assemblage in our analysis. However, in many cases, the brown-colored patches represent the enclosing boundary to the moderate G/NIR grains we identify as olivine. This boundary region is estimated to account for 26.8% area coverage, and the dark-brown regions with low G/NIR ratio that we consider fully altered regions accounts for 15.6% area coverage, consistent with the areal extent of nondiffracting secondary phases in the combined x-ray analysis patches. Correspondingly, these boundary levels constrain the areal coverage of olivine and lightly altered or partially replaced olivine. In areas where overlapping XRF, XRD, and color information exists, we find that some brown patches exhibit diffraction peaks indicative of a coarsely crystalline phase and have chemical compositions consistent with olivine.

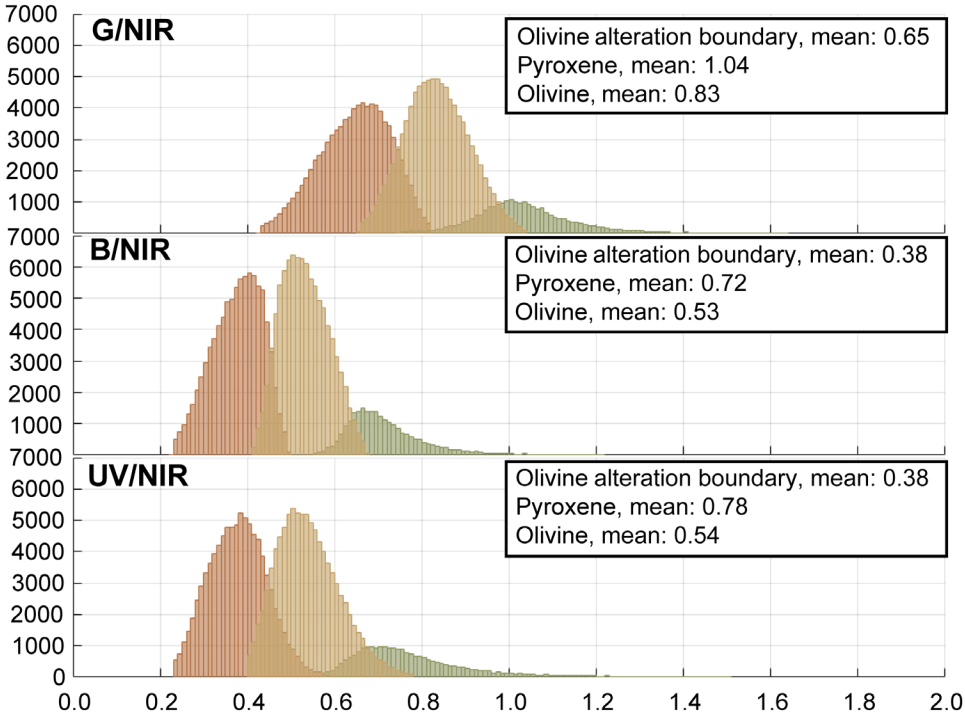

Fig. 7. Multispectral band ratio classification. The three main regions (pyroxene, olivine plus mesostasis, and alteration/secondary) classified based on band ratio histograms. Pyroxene regions show no overlap with alteration regions, indicating that pyroxene is largely unaltered. The boundary between the olivine plus mesostasis region and the altered region is not as well defined but shows a broad transition. As a lower boundary for the fully altered regions, individual thresholds of 0.67, 0.42, and 0.40 for G/NIR, B/NIR, and UV/NIR, respectively, and 0.82, 0.50, and 0.57 are used as upper boundary levels to consider fully altered regions.

Thus, we conclude that relatively unaltered olivine and mesostasis constitute about 46% areal abundance, lightly altered or partially replaced olivine constitutes 27% areal abundance, and secondary minerals account for 16%; these results are consistent with the previous estimates that do not distinguish lightly altered olivine from olivine (*25*). If mesostasis accounts for 10% of the rock (*25*), then about half of the original olivine in the Dourbes patch has been completely replaced or partially altered.

Comparison with Raman and UV fluorescence spectroscopy (SHERLOC)

Inferred carbonate and sulfate minerals are consistent with Raman spectroscopic identification of these phases (*35*). SHERLOC did not detect perchlorate in Dourbes; however, it is not known whether SHERLOC sampled a spot with enough Cl-bearing phase to exclude its presence. From the Raman peak width coupled with WATSON observations of the sample during SHERLOC analyses, crystalline size of the carbonate and sulfate phases appears to be in some areas much lower than the resolution of the PIXL instrument (~120 μm).

DISCUSSION

Primary igneous origin

Crystallinity results, combined with the texture and chemistry data, support the interpretation of a primary igneous origin for the Bastide member rocks of the Séítah formation (*25*). Multiple origins are possible to explain the granular texture comprising olivine grains of similar size. The crystalline interstitial regions, particularly the poikilitic texture of coarse single pyroxene grains as revealed by the crystal domain analysis, are inconsistent with a sedimentary origin. The texture and chemistry are most consistent with those observed in cumulate rocks formed by slow cooling of an igneous melt, whether as a thick lava, a shallow magmatic intrusion, or a large impact melt sheet (*25*).

Textural relationships between primary igneous minerals and secondary minerals are also consistent with an igneous protolith, not a cemented sandstone, conglomerate, or pyroclastic rock. Domain clustering analysis indicates that apparently disconnected small olivine grains separated by secondary phases were originally single domain crystals that have been infiltrated and dissected by fluids (Fig. 6B). Partial or complete replacement of olivine grains by low-(Fe,Mg)-silicate and (Fe,Mg)-carbonate similarly suggests that the distribution of these minerals along olivine grain boundaries reflects partial dissolution and replacement of olivine, not cementation of loose grains.

Alteration processes and paragenetic sequence

Compositional and textural evidence for dissected olivine grains, as well as secondary material confined to intra- and interparticle pore space, indicate that some of this material was derived from the interaction between water and a primary silicate mineral assemblage dominated by olivine. These data also show that roughly half of the olivine in the rock was unmodified as a result of this and subsequent stages of aqueous interaction; this contrasts strongly with terrestrial examples of altered olivine-bearing rocks that seldom preserve olivine in similar abundances (*40*). Because the dissolution rate of olivine and, therefore, the lifetime of a given olivine grain vary strongly as a function of pH and temperature (*41*), these observations likely

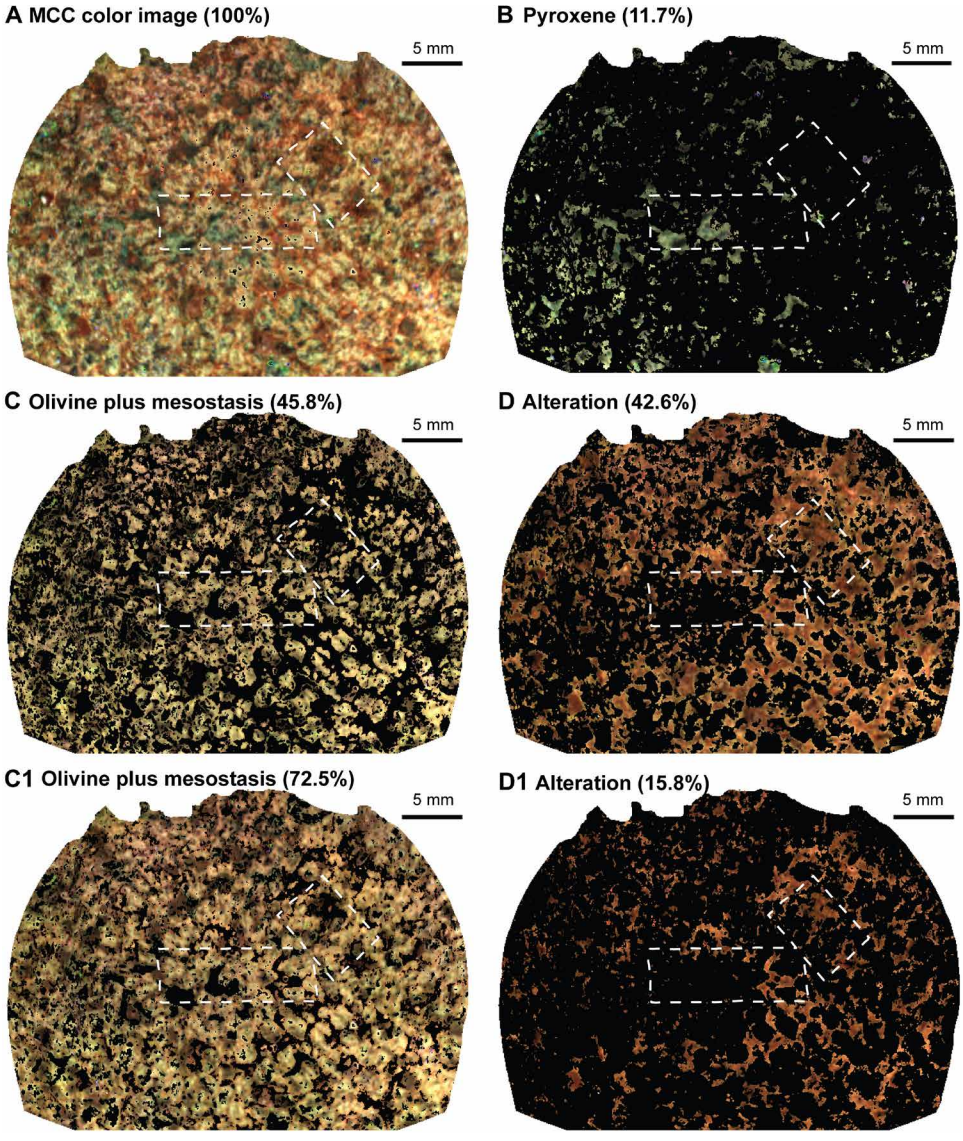

Fig. 8. Multispectral classification. Dourbes target classified into three main regions (pyroxene, olivine and mesostasis, and mesostasis). These images show the classified regions individually in the field of view of the MCC. (**A**) the full abraded target cleared of dust, (**B**) the pyroxene regions, (**C**) the olivine and mesostasis regions, and (**D**) the alteration regions. On the basis of individual set threshold of the ratio levels, the fully altered regions are separated from the boundary olivine-alteration regions. The resulting distribution is shown in (C1) and (D1) for the olivine and mesostasis plus alteration regions, respectively.

reflect a style of water-rock interaction that proceeded at relatively low temperature or was limited in duration, water volume, or both.

The presence of low Fe-Mg silicates throughout these targets and their spatial distribution further supports the hypothesis that the olivine from the Séítah protolith experienced low-temperature aqueous alteration. Poorly crystalline or x-ray amorphous silicate containing cations (*42*, *43*), often precipitated with secondary carbonate, is commonly produced through aqueous alteration of terrestrial peridotites, serpentinites, and basalts (*42*, *44*, *45*) and experimental low-temperature (<200°C) alteration of olivine (*43*, *46*–*48*). In both natural and synthetic systems, these amorphous silicates precipitate around the olivine grains, whereas carbonate fills fractures and pore spaces surrounding and adjacent to the olivine (*42*–*44*, *46*–*50*) in a manner consistent with textures observed among primary and secondary minerals in Dourbes. These alteration assemblages form when CO_2-rich fluid dissolves olivine and releases both silica and cations (Mg, Fe, or both) into the fluid (*43*, *46*–*48*), with amorphous silicate precipitating from solution to form linings or reaction rims around the olivine (*43*, *44*, *46*–*48*) or precipitating in fractures and pore spaces around and adjacent to the olivine (*42*). As this precipitation proceeds, some of the cations released from solution may become incorporated into, or help nucleate the precipitation of, the amorphous silicate (*42*, *43*). Following the formation of this silica layer, the remaining cations released into solution react with the dissolved CO_2 to form carbonates in the pore spaces and fractures within and around the olivine (*44*, *48*, *51*).

The (Fe,Mg)-carbonate, as well as its relationship to olivine, is also consistent with water-limited and/or low temperature alteration.

The composition of the carbonate mirrors that of the olivine, which, in turn, suggests that it crystallized from a solution with approximately equal Mg and Fe activities. The thermodynamics of carbonates along the Fe-Mg compositional join indicate that the solid phase carbonate composition that is in equilibrium with a fluid of approximately equal Mg and Fe activities should be dominantly ferroan (*52*). Thus, the similarity between carbonate and olivine composition reflects a kinetically driven process whereby $Fe_{0.45}Mg_{0.49}Ca_{0.06}CO_3$ nucleated from a strongly supersaturated fluid but did not interact with the fluid long enough or at high enough temperature to recrystallize to ferroan carbonate. This inference is consistent with a lack of diffracted x-rays from the carbonate phase, which suggests that it is finely crystalline (≤20 to 30 μm) or amorphous, in turn, reflecting nucleation-dominated growth and therefore precipitation at a state of high supersaturation, and limited subsequent crystal growth (*53*).

Textural and compositional observations from the Dourbes abraded targets collectively indicate that a later fluid, distinct from that which initially generated the poorly crystalline low-(Fe,Mg)-silicate and (Fe,Mg)-carbonate phases, infiltrated the rock and deposited sulfate minerals. Specifically, the Mg-rich sulfate we observed does not appear to be accompanied by an equivalent quantity of Fe-bearing sulfate or another mineral form (e.g., Fe-oxide), suggesting that the deposition of this phase is not from the fluids that produced carbonate and silicate. The interaction with olivine appears to have released roughly equivalent proportions of Fe and Mg, as reflected in the chemistry of carbonates and secondary silicate. Small, concentrated areas of Ca-sulfate, which are accompanied by Mg-sulfate, also cannot originate from olivine alteration, as olivine is a Ca-free mineral phase. We therefore propose an exogenous origin for Mg- and Ca-sulfate observed in Dourbes, delivered by a second pulse of fluid that migrated through the rock. These sulfate phases appear to fill the central portions of altered areas of the rock (Fig. 4), implying that they migrated into altered areas, perhaps filling in the remaining pore space that was left unfilled after secondary silicates and carbonates precipitated around and between olivine grains in an earlier stage of water-rock reaction.

Last, we observe perchlorate that appears to be spatially associated with all the previously described secondary phases (Figs. 1F and 4), as well as lower-level Cl-enrichment in some olivine, suggesting an overprinting textural relationship. Similar to the Mg-sulfate and Ca-sulfate, this Na- and Cl-bearing phase cannot have been derived from complete or partial dissolution of olivine, which has no Na in its structure, and possibly not from interaction with any mineral in the Dourbes patch, given the overall low abundance of mesostasis and its apparently unaltered composition (*25*). Given its overprinting textural relationship to sulfates, carbonates, and secondary silicates, we propose that this perchlorate represents the third and final stage in the aqueous history of the Dourbes scan area, characterized by deposition of chlorine/oxychlorine in the rock.

Environmental setting of alteration and potential for habitability

Together, the composition, crystallinity, and textural relationships described above among primary and secondary materials in the Bastide member of the Séítah formation imply limited water/rock ratios, limited integrated time scales of aqueous alteration, or some combination of both. We propose a three-stage sequence of interaction with environmental fluids characterized by varying composition, ability to dissolve olivine, and Fe-oxidizing capacity to explain the paragenetic sequence of rock alteration observed in the Dourbes abraded patch (Fig. 9). Each of these stages would have provided challenges and opportunities for habitability, potential for organic matter production (abiotic or biotic), and preservation of biosignatures.

In the first stage of alteration, olivine was partially dissolved and replaced (Fig. 9B). Although we cannot estimate theoretical constraints on temperatures during this alteration stage, carbonate mineral compositions and analogy to terrestrial systems that produce similar secondary silicates imply temperatures well below 200°C (*43*, *46*–*48*). The alteration process required sufficient dissolved inorganic carbon (DIC) to precipitate carbonate mineral, which indicates that the fluid medium was not derived from a deep groundwater source that had lost its DIC to earlier water rock reaction [e.g., (*54*)]. Together with the inference that observed carbonate minerals formed at low temperatures, this is consistent with meteoric water or water derived from a shallow aquifer system. The nearly identical Mg/Fe ratio of the carbonates to that of both the low-(Fe,Mg)-silicate and the olivine they are derived from provides a strong indication that the fluids that interacted with olivine were not capable of oxidizing Fe(II). In an Fe-oxidizing system, the carbonate would be expected to be Fe-poor, with Mg-Ca carbonate physically separated from Fe-oxides by the extreme solubility differences between carbonate and Fe-oxide minerals. Thus, although the current data suggest minor oxidation of olivine and secondary Fe-bearing materials, this oxidation was likely not significantly associated with the earliest stage of rock alteration by water.

Similarly, the presence of (Fe-Mg)-carbonate and the lack of accompanying Fe-oxide minerals likely imply very little, if any, in situ production of H_2 during this stage of alteration in the Séítah formation. In anoxic, H_2-producing systems, the reduction of H_2O by Fe(II) results in the precipitation of mixed-valence (magnetite) and/or ferric (hematite, goethite) iron oxides (*55*). H_2 and Fe(III) can both subsequently provide energy sources for subsurface microbial communities [e.g., (*56*)] or to abiotic organic synthesis reactions (*57*). In the absence of substantial locally produced energy sources, any putative microbial life that was present at the time during which this early olivine alteration was occurring would have either been low productivity or have had to receive its energy from fluids or gases that were supplied from outside the system. The limited water/rock ratios required for observed carbonate formation further imply that the supply of both water and energy sources was likely low and episodic, so habitability was likely also limited and sporadic (*58*, *59*) during this earliest stage of rock alteration.

The emplacement of Mg- and Ca-sulfate minerals in the internal portions of altered areas of the Dourbes scan is interpreted to reflect a second stage in the aqueous history of the Séítah formation (Fig. 9C). The amount of time that passed between olivine alteration and carbonation and sulfate emplacement cannot be constrained. Unlike the initial stage of carbonation, however, this process of Mg-Ca-sulfate emplacement appears to have affected both the Séítah formation and the overlying Máaz formation (*17*, *35*), suggesting that the fluid source of sulfate mineralization affected both lithologic units. Unlike the first alteration stage, olivine does not appear to have been dissolved during this stage. Instead, sulfate minerals were precipitated into the centers of areas already containing alteration minerals. Moreover, the composition of the sulfates in Dourbes implies an exogenous origin rather than through direct interaction between a sulfate-bearing fluid and the olivine of the Séítah formation. The

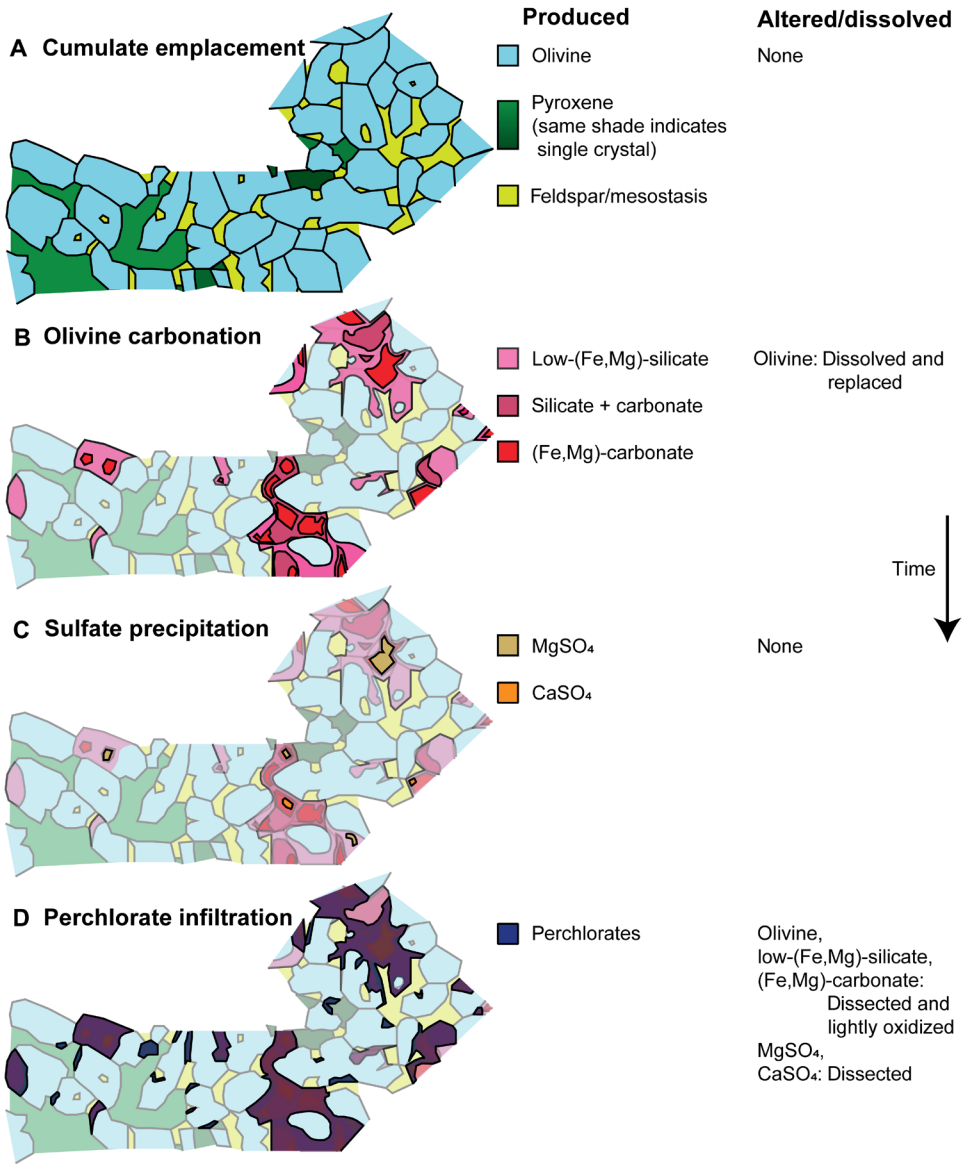

Fig. 9. History of the Dourbes abrasion patch. Emplacement of olivine cumulate in the Bastide member of the Séítah formation (**A**) was followed by three successive stages of alteration by or precipitation from water rich in carbonate (**B**), sulfate (**C**), or perchlorate (**D**). Time progresses from top to bottom.

presence of sulfate minerals, particularly Mg-sulfate, indicates that the fluids that precipitated these phases were concentrated saline brines, which are also unlikely to dissolve olivine (*41*).

These fluids become concentrated by evaporative or freezing processes that can take place in the vadose zone or by downward percolation of concentrated brines from an overlying water column that itself was subjected to evaporation or freezing. No bottom-growth precipitates or bedded evaporites have been observed in the crater floor stratigraphy explored thus far; these deposits would likely have formed from surface evaporation sufficient to drive Mg-sulfate-brines into the lake subsurface. Moreover, although it is possible that these deposits could yet be found, it is unlikely that only sulfate mineral–saturated brines would have penetrated to the Bastide member during repeated wetting and drying of a lake. Migration of less saline fluids would have produced some alteration of the preexisting primary and secondary mineral assemblage during this stage of aqueous interaction, and this is not observed. In the absence of evidence for precipitation from surface-derived evaporative fluids, vadose zone brine migration through both the Séítah and Máaz formation is a likely emplacement mechanism for these minerals.

Organisms in highly concentrated brines capable of depositing sulfate minerals would have required some degree of halotolerance, but this tolerance of selected bacterial isolates for martian brines has now been shown for $MgSO_4$, NaCl, and oxychlorine salts under saturation conditions, including deliquescence (*60*). We cannot place any strong constraints on the oxidizing or reducing potential of the sulfate-emplacing fluids, so energy sources for any contemporaneous rock-hosted microbial communities are unconstrained. However, despite the relatively low biosignature preservation potential of igneous rocks (*61*), sulfate minerals associated with these rocks have

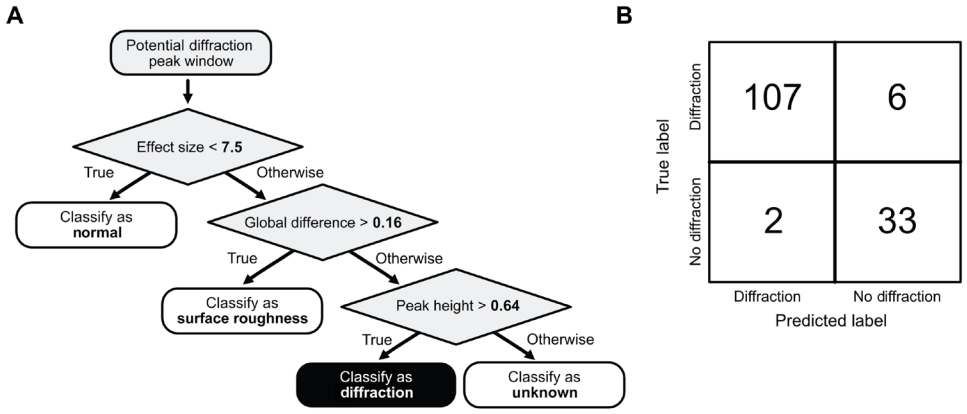

Fig. 10. Automated diffraction identification. At the left, the learned decision tree (**A**) splits each data instance into a predicted class based on a series of parameter-value tests. The learned tree classifies spectral peaks as normal, diffraction, surface roughness, or—to minimize false positives—as unknown. At the right, (**B**) the error analysis of the decision tree using the subject matter expert–labeled data. Columns show the predicted labels, and rows show the true labels. Correct predictions are along the diagonal.

higher biosignature preservation potential and may preserve organic materials (*62*–*64*). Abiotically formed organic material has been described in 13 martian meteorites associated with aqueous alteration reactions that include serpentinization and carbonation (*57*, *65*), and organic material in several samples analyzed in situ by the Mars Science Laboratory (MSL) Curiosity rover was likely sourced from abiotic photosynthesis, meteorite infall, and mantle sources (*66*); it is likely that these mechanisms provide a parsimonious explanation for the organic material described by Scheller *et al.* (*35*). Nonetheless, it is not implausible that the organic material detected by SHERLOC in abraded Séítah formation rocks associated with sulfate salts (*35*) may reflect in situ production by chemoautotrophic/chemolithotrophic subsurface communities present during this second stage of rock alteration, potentially with subsequent alteration of the organic material itself. Ground-based analyses on the samples collected in this unit and returned by the Mars Sample Return mission will be required to determine a composition of the detected organic material that is sufficiently detailed to determine its origins. Furthermore, in situ comparison to salt mineral assemblages in other crater fill lithologies and locations could also provide constraints on the origin of this organic material.

Last, we observe a general enrichment in chlorine across areas in the Dourbes scans associated with primary and secondary mineral phases. Using chemical constraints from PIXL, we attribute this enrichment to the presence of sodium perchlorate but cannot unequivocally rule out the presence of NaCl or other lower oxidation state oxychlorines, which are expected (*67*). The presence of oxychlorines would be entirely consistent with their identification at the Phoenix and Curiosity mission landing sites [e.g., (*68*, *69*)]. The martian SNC meteorites (Shergottites, Nakhlites, Chassignites) also exhibit Cl enrichments in association with areas of preterrestrial aqueous alteration [e.g., (*70*)]. This stage of alteration (Fig. 9D) affected much of the olivine and alteration assemblage that was already present but does not appear to have dissolved much olivine or any pyroxene, suggesting low water-rock ratios. There is also an apparent textural relationship between Cl enrichment, reddish/brown coloration, and elevated FeO/(SiO_2 + MgO) in Dourbes (Figs. 4 and 8D1 and fig. S4), which may indicate a role for oxychlorine species in oxidizing ferrous iron–bearing minerals; laboratory studies indicate that chlorate, not perchlorate, is an effective Fe oxidizer in solution (*71*). The general preservation of similar Fe/Mg ratios in olivine, low-(Fe,Mg)-silicate, and (Fe,Mg)-carbonate despite color evidence for some iron oxidation during this alteration stage is also consistent with low water-rock ratios. By analogy with terrestrial occurrences of perchlorate accumulation, e.g., in the Atacama Desert of Chile (*72*, *73*), perchlorate is thought to be derived from photochemical processes occurring in the martian atmosphere that oxidize chlorine to higher oxidation state oxychlorine species. Extreme chlorine isotope fractionation in rocks and soils measured by the SAM instrument (Sample Analysis at Mars) onboard Curiosity further attest to a late stage, atmospherically derived origin (*26*). The migration of oxychlorine-bearing fluids into rock fractures and pores under Amazonian environmental conditions is likely aided by freezing point depression in oxychlorine-bearing fluids, which permits them to be stable as liquids, even in the modern climate (*74*). Chlorates and perchlorates are deliquescent, and brines form rapidly when the salts are in contact with water or water ice. The deliquescence of hygroscopic minerals could have provided a local and transient source of liquid water that would have been available for microorganisms in Jezero (*60*).

The regional association of the Séítah formation outcrops with olivine and carbonate having similar Mg/Fe ratios (*28*, *31*) to those observed in Dourbes may imply an early regional weathering style regime of olivine alteration associated with groundwater or meteoric fluid at low water-rock ratio, although diverse mechanisms and sources of CO_2 acting across this broad region cannot be ruled out by this analysis. However, given evidence for standing surface water within Jezero crater for part of its history (*14*, *15*), it is perhaps unexpected that alteration of the Bastide member was not more extensive. This may reflect the past presence of protective rock strata, since eroded, that effectively prevented fluid migration from the overlying lake into the Séítah formation. Alternatively, the lake could have been only episodically filled with water, potentially because of ephemeral discharge from feeder channels or because of predominantly cold conditions that caused water entering the crater to freeze at most times, thus limiting extensive water-rock interaction. Last, it is possible that Séítah rocks were emplaced as a shallow intrusive body after lake activity and formation of the delta and that some or all the activity that produced carbonate minerals in the

regional olivine-carbonate unit occurred after lacustrine activity in Jezero crater.

MATERIALS AND METHODS

Mineral stripping analysis

To map saline mineral distributions and to remove their compositions from mixing models between other minerals, we first assigned measured oxides to merrillite and then to $CaSO_4$ and $MgSO_4$, $NaClO_4$, and Fe,Cr,Ti-spinels, subtracting from the available pool of oxides with each step. We refer to this process as mineral stripping because it mathematically removes accessory minerals from each PIXL measurement spot, successively revealing other minerals present in the same spot.

For merrillite removal, we assume a composition of $Ca_9NaMg(PO_4)_7$ and assign as much CaO, Na_2O, MgO, and P_2O_5 to merrillite as possible given the amount of stoichiometrically limiting oxide present, typically (P_2O_5). The amount of each oxide assigned to merrillite was then subtracted from the available pool of CaO, Na_2O, and MgO at each measurement spot. Next, we assigned as much CaO, MgO, and SO_3 to $CaSO_4$ and $MgSO_4$ as possible, with resultant $CaSO_4/(CaSO_4 + MgSO_4)$ approximated by setting it to be equal to the initial ratio of CaO/(CaO + MgO). Once again, CaO and MgO were subtracted from the available pool at each measurement spot. Next, as much Na_2O and Cl were assigned to $NaClO_4$ as possible, assuming an apparent detected molar ratio of $Na_2O/Cl = 0.309$ because of absorption of Na fluorescence by O in perchlorate. Last, FeO was assigned to Fe,Cr,Ti-spinels having Fe/(Cr + Ti) = 1. This was approximately the minimum value observed by previous analyses of spinels in this rock (*25*), so this step is likely conservative in its mathematical removal of FeO from the rest of the rock. Maps illustrating the effects of mineral stripping are included in the Supplementary Materials (fig. S3). $MgSO_4$, $CaSO_4$, and $NaClO_4$ calculated in corresponding stripping steps were mapped as proxies for the distributions of these minerals (Figs. 1 and 4).

Mineral mixing modeling

The PIXL measurement spot is 120 μm in diameter [full width at half maximum (FWHM) intensity] at 8 keV, with larger spot sizes at lower energies (*11*). This energy dependence in spot size effectively gives PIXL a larger excitation and collection area for x-rays associated with elements having lower atomic numbers (e.g., Na, Mg, Al, and Si) than for those with higher atomic numbers (e.g., K, Ca, and Fe). This results in apparent mixing relationships between neighboring mineral grains that are slightly nonlinear, making identification of grain contacts complex.

To estimate the energy-dependent variation in spot size and its effect on mixing relationships, we assumed that spot size (FWHM) varies linearly with photon energy between 1 keV (Na K_α) and 8 keV. We then approximated elemental concentrations observed while moving the PIXL spot over a mineral boundary as an error function of distance from the boundary with width equal to FWHM/2.35, where FWHM was calculated at the $K_{\alpha 1}$ for the respective element. We modeled mixing relationships for Dourbes olivine, pyroxene, feldspar, (Fe,Mg)-carbonate, and low-(Fe,Mg)-silicate and plotted the results on a Si-Mg-Ca ternary diagram, together with the observed data (fig. S4). Last, we visually fit the resultant mixing curves by holding the spot size at 8-keV constant and varying the spot size at 1 keV. The resultant best-fit set of mixing relations implies effective beam sizes (FWHM) for Na, Mg, Al, Si, K, Ca, and Fe of 230, 220, 220, 220, 190, 190, and 140 μm, respectively.

We used the best-fit beam sizes to model mixing between theoretical stoichiometric endmembers. Because the widths of (Fe,Mg)-carbonate patches and feldspar grains in Dourbes are similar to the effective spot sizes of Na, Mg, Al, and Si, it is likely that every spot including those minerals also had compositional contributions from other minerals. This fact explains the lack of measurement spots composed of stoichiometric feldspar or (Fe,Mg)-carbonate. We therefore extrapolated compositions for (Fe,Mg)-carbonate and feldspar by extending mixing lines to low SiO_2 and low MgO + FeO compositions, respectively.

Machine learning detection of diffraction peaks for crystallinity

The large number of x-ray spectra contained in each PIXL scan guided us to consider an automated approach to identify diffraction peaks. While previous researchers have characterized diffraction and considered its removal when known to be present (*39*), the absence of a generalized, detector-agnostic, performance-benchmarked algorithm led us to introduce one, which we describe in this section. Because our objectives included an accurate characterization of its performance, we chose to follow a supervised approach, which would involve training and testing with a set of instances whose classes are known. Supervised classifiers are also widely applied across the sciences because they are more robust than model-based approaches.

Our supervised approach started with the creation of a ground truth dataset that we could use to train the algorithms that we would use and whose labels could allow us to assess the efficacy of the trained algorithms. We recruited three subject matter experts and presented each with a series of spectra to label that contained a diversity of diffraction peak and surface roughness characteristics from a diversity of samples and instruments. These included two terrestrial rock samples from a collection at the Jet Propulsion Laboratory, named Crystal Geyser and King's Court, which were scanned with the PIXL engineering model instrument; another terrestrial rock sample from the same collection, named the Spherical Conglomerate Rock, scanned with the PIXL flight instrument before launch; and scan data collected on Mars with the PIXL flight instrument on the target named Bellegarde. We also injected random peaks to collect true-negative examples. This training dataset consisted of 102 anomalies, of which 72 were determined to be diffraction, 15 were surface roughness, and 13 were nothing or unknown.

To increase the overall system accuracy, we designed a series of features to accompany each labeled instance that could provide statistical descriptions to characterize its distinguishing characteristics (*75*). Because sensor noise often creates differences between sensor channels that might look like diffraction, we first chunk each pair of spectra into 0.2-keV segments (similar to the measured energy resolution of the PIXL detectors) and use those as the starting point for feature design. First, because even chunked spectral segments contain sensor noise that is not diffraction, we added an effect size feature, which uses the *t*-statistic (and not the *P* value) from a paired *t* test between the A/B spectral chunks to evaluate the hypothesis that the difference in each detector's intensity over the window is due to chance. Second, because diffraction manifests as a difference between peak intensity, we calculate the peak height difference, or the absolute intensity difference between the two detectors at the center of each window. Last, because another spectral anomaly, surface

roughness, manifests as a spectra-wide difference in height between the readings in both sensors, we calculate the average absolute window difference, or global difference between the detectors across the entire spectra. Each chunk of each pairwise spectra are then encoded in a tuple using the following format that forms the input to the classification algorithm

<windows center channel, effect size, peak height difference, global difference>

To ensure that the algorithm's output could be easily understood by scientists, we elected to use a decision tree classifier (*76*). A decision tree splits each data instance into a predicted class based on a series of parameter-value tests. The algorithm learns the parameters and ordering that best distinguish the various classes. We trained the decision tree using leave one out cross-validation (*77*) on the training dataset, and it learns a very simple series of splits (Fig. 10A) to classify spectral peaks as normal, diffraction, surface roughness, or—to minimize false positives—as unknown.

To evaluate the diffraction peak classifier on PIXL data from Mars rocks, we asked three different subject matter experts to manually classify randomly selected spectra from the Dourbes targets. In this testing dataset, 148 randomly sampled spectra had a consensus of labels, and the classifier correctly identified 94.6% of the examples, with only two false negatives and six false positives (Fig. 10B).

Crystal domain clustering analysis

The peak energy and height for all diffraction peaks identified using the algorithm discussed previously were modeled as Gaussian peaks with a width corresponding to 100 eV producing a spectrum of the diffraction detected for each measurement spot. The diffraction spectra clustered into *n* clusters for olivine and pyroxene regions for each dataset, where *n* was chosen as the maximum value before two clusters look visually similar. The resulting clusters in each case are shown in fig. S2, where the bold line refers to the cluster center and the thin lines correspond to the spectra that are in each cluster. Each cluster is presented in Fig. 6 as an individual color. Where there is misalignment between grains of the same mineral as described below the clusters are presented as similar colors (Fig. 6B).

The PIXL incident x-ray beam has a convergence angle of approximately 8°, while the detectors each have an acceptance angle of approximately 22°. Combined with the polychromatic radiation, this results in the Bragg condition being satisfied for a given lattice spacing over a range of relative crystal orientations. As a result, two grains of the same mineral can have a relative tilt of up to 8° before the reflection is no longer detected. These relative angular displacements would result in an energy shift of the peak recorded by PIXL approximately 100 eV at 10 keV (Supplementary Materials). As a result, clusters with similar diffraction peaks shifted in energy by less than 100 eV represent grains of the same mineral where there is a misalignment of less than 8° between two grains (fig. S2).

Diffraction dependence on crystalline domain size and orientation

There are two cases in which a crystalline material may not produce diffracted x-rays detected by PIXL: (i) The crystalline domains are too small to produce sufficient diffracted x-rays for detection or (ii) no crystal lattice is oriented such that x-rays are diffracted back to one of PIXL's two detectors. To evaluate the circumstances under which either of these cases could affect PIXL measurements, we conducted experiments with varying crystal domain sizes and predicted theoretical diffraction detections for randomly oriented crystals.

To determine the effect of crystallite size on diffraction peak intensity, the PIXL Breadboard at JPL was used to analyze halite (NaCl) crystals. Halite crystals were partially crushed using a steel puck mill before being passed through steel sieves into 45- to 90-, 90- to 180-, 180- to 300-, 300- to 500-, and 500- to 1000-μm size fractions. Using an x-ray tube energy of 28 keV and 40 μA, the x-ray beam was focused through the polycapillary optic onto the surfaces of NaCl samples placed in Teflon sample holders. Five, spatially separated, 30-s-long integrations were obtained for each of the sample size fractions (fig. S5).

Because of the fixed relationship between the PIXL x-ray source, detectors, and the sample, there is a probability that diffraction from a single crystal will be missed, leading to an ambiguity in assigning crystalline and amorphous phases. The number of reflections recorded in single-crystal diffraction is proportional to the unit cell volume. We therefore use halite as a test case due to its relatively small unit cell volume of 179.4 $Å^3$. The process is as follows. Miller indices for all (*hkl*) from −50 to 50 were generated, and the vector orthogonal to the crystal plane (hereby referred to as the diffraction vector, *g*) along with the lattice plane spacing, *d*, were calculated. For a given x-ray beam-crystal orientation and lattice plane, the energy *E* that satisfies the Bragg condition can be calculated as follows (*78*)

$$E = \frac{hc}{2\,d_{hkl}[\cos\delta\sin\alpha + \sin\delta\cos\alpha\cos(\gamma - \varphi)]}$$

where *h* is Planks constant, *c* is the speed of light, and d_{hkl} is the d-spacing for the (*hkl*) crystallographic plane. The angles δ, γ, and (π - α), φ define as the polar and azimuthal angles of the diffraction vector *g* and the direction of the incident x-ray beam relative to the crystallographic c axis and together define the relative angle between the two. For an energy in keV, *hc* reduces to approximately 12.398. This gives a set of diffraction vectors (*g*) each with its required energy *E*. Diffraction in PIXL is generally observed within the energy range of 1 to 15 keV, and therefore, diffraction vectors with an energy outside this range are discarded. Reflections with zero or negligible intensity based on the structure factor *F* were also discarded (*79*). The resulting diffraction vectors for a single x-ray beam-crystal orientation are depicted in Fig. 5A. The location of PIXL's detectors, the angular acceptance of the detectors, and the angular convergence of the x-ray beam (*11*) determine the range of diffraction vectors that will result in diffraction being recorded in either detector, with the relationship between the diffraction vector and detectors shown in Fig. 5B. The number of diffraction vectors that are detected by PIXL's geometry and energy detection limits were calculated for 10,000 randomly chosen x-ray beam-crystal orientations, with the results shown in Fig. 5C, with an example of diffraction recorded from each of PIXL's two detectors shown in Fig. 5D.

Multispectral imaging

PIXL's Optical Fiducial System (OFS) consist of three subsystems: the MCC, the structured light illuminator (SLI), and the flood light illuminator (FLI). At nominal standoff distance, 25.5 mm, the MCC captures images over an area of 39 mm by 31 mm, with a pixel resolution of 50 μm. The FLI enables the OFS multispectral capabilities with its 24 monochrome light-emitting diodes (LEDs) evenly

distributed into four different wavelengths: NIR (735 nm), green (G, 530 nm), blue (B, 450 nm), and UV (385 nm).

The raw multispectral images are individually dark-level corrected, to ensure common zero level, and flat-field corrected, to provide evenly distributed light intensity. The SLI measurements provide the three-dimensional topography information required in the creation of the flat fielding compensation profile (*11*, *80*). The profile is made from a series of calibration images captured on ground of a spectrally flat target at standoff distances ranging from 22 to 72 mm. To make the four channels comparable, the individual images are additionally compensated for varying shutter time, spectrally dependent charge-coupled device sensitivity, and specific radiated power of the monochrome LEDs.

This image processing results in radiometrically corrected multispectral images that directly enable the creation of color images composed of the four bands. Furthermore, the four bands provide 12 different ratio maps by dividing the individual color channels with one another.

The radiometric calibrated image can be used for classification by defining a number of different classes and forcing each pixel to classify into one of the defined groups. From the XRF data, three overall groups are defined: pyroxene, olivine, and altered, corresponding to green, light toned, and brown/red, respectively, in the NIRGB image. This classification, from the XRF scan, is extrapolated to cover the full MCC field of view. The given mineral can then be quantified into a rock volume percentage.

SUPPLEMENTARY MATERIALS

Supplementary material for this article is available at https://science.org/doi/10.1126/sciadv.abp9084

REFERENCES AND NOTES

1. M. H. Carr, *The Surface of Mars* (Yale Univ. Press, 1981), pp. 232.
2. B. L. Ehlmann, C. S. Edwards, Mineralogy of the Martian surface. *Annu. Rev. Earth Planet. Sci.* **42**, 291–315 (2014).
3. J. P. Grotzinger, R. E. Milliken, in *Sedimentary Geology of Mars*, J. P. Grotzinger, R. E. Milliken, Eds. (SEPM Society for Sedimentary Geology, 2012), vol. 102, pp. 1-48.
4. R. E. Arvidson, S. W. Ruff, R. V. Morris, D. W. Ming, L. S. Crumpler, A. S. Yen, S. W. Squyres, R. J. Sullivan, J. F. Bell III, N. A. Cabrol, B. C. Clark, W. H. Farrand, R. Gellert, R. Greenberger, J. A. Grant, E. A. Guinness, K. E. Herkenhoff, J. A. Hurowitz, J. R. Johnson, G. Klingelhöfer, K. W. Lewis, R. Li, T. J. McCoy, J. Moersch, H. Y. M. Sween, S. L. Murchie, M. Schmidt, C. Schröder, A. Wang, S. Wiseman, M. B. Madsen, W. Goetz, S. M. McLennan, Spirit Mars rover mission to the Columbia Hills, Gusev Crater: Mission overview and selected results from the Cumberland Ridge to Home Plate. *J. Geophys. Res.* **113**, E12S33 (2008).
5. E. B. Rampe, D. F. Blake, T. F. Bristow, D. W. Ming, D. T. Vaniman, R. V. Morris, C. N. Achilles, S. J. Chipera, S. M. Morrison, V. M. Tu, A. S. Yen, N. Castle, G. W. Downs, R. T. Downs, J. P. Grotzinger, R. M. Hazen, A. H. Treiman, T. S. Peretyazhko, D. J. Des Marais, R. C. Walroth, P. I. Craig, J. A. Crisp, B. Lafuente, J. M. Morookian, P. C. Sarrazin, M. T. Thorpe, J. C. Bridges, L. A. Edgar, C. M. Fedo, C. Freissinet, R. Gellert, P. R. Mahaffy, H. E. Newsom, J. R. Johnson, L. C. Kah, K. L. Siebach, J. Schieber, V. Z. Sun, A. R. Vasavada, D. Wellington, R. C. Wiens; the MSL Science Team, Mineralogy and geochemistry of sedimentary rocks and eolian sediments in Gale crater, Mars: A review after six earth years of exploration with *Curiosity*. *Geochemistry* **80**, 125605 (2020).
6. R. E. Arvidson, J. W. Ashley, J. F. Bell III, M. Chojnacki, J. Cohen, T. E. Economou, W. H. Farrand, R. Fergason, I. Fleischer, P. Geissler, R. Gellert, M. P. Golombek, J. P. Grotzinger, E. A. Guinness, R. M. Haberle, K. E. Herkenhoff, J. A. Herman, K. D. Iagnemma, B. L. Jolliff, J. R. Johnson, G. Klingelhöfer, A. H. Knoll, A. T. Knudson, R. Li, S. M. McLennan, D. W. Mittlefehldt, R. V. Morris, T. J. Parker, M. S. Rice, C. Schröder, L. A. Soderblom, S. W. Squyres, R. J. Sullivan, M. J. Wolff, Opportunity Mars Rover mission: Overview and selected results from Purgatory ripple to traverses to Endeavour crater. *J. Geophys. Res.* **116**, E00F15 (2011).
7. S. M. McLennan, J. P. Grotzinger, J. A. Hurowitz, N. J. Tosca, The sedimentary cycle on early Mars. *Annu. Rev. Earth Planet. Sci.* **47**, 91–118 (2019).
8. K. L. Siebach, M. B. Baker, J. P. Grotzinger, S. M. McLennan, R. Gellert, L. M. Thompson, J. A. Hurowitz, Sorting out compositional trends in sedimentary rocks of the Bradbury group (Aeolis Palus), Gale crater, Mars. *J. Geophys. Res.* **122**, 295–328 (2017).
9. S. J. VanBommel, R. Gellert, J. A. Berger, J. L. Campbell, L. M. Thompson, K. S. Edgett, M. J. McBride, M. E. Minitti, I. Pradler, N. I. Boyd, Deconvolution of distinct lithology chemistry through oversampling with the Mars Science Laboratory Alpha Particle X-Ray Spectrometer. *X-Ray Spectrom.* **45**, 155–161 (2016).
10. J. A. Berger, M. E. Schmidt, R. Gellert, N. I. Boyd, E. D. Desouza, R. L. Flemming, M. R. M. Izawa, D. W. Ming, G. M. Perrett, E. B. Rampe, L. M. Thompson, S. J. V. VanBommel, A. S. Yen, Zinc and germanium in the sedimentary rocks of Gale Crater on Mars indicate hydrothermal enrichment followed by diagenetic fractionation. *J. Geophys. Res.* **122**, 1747–1772 (2017).
11. A. C. Allwood, L. A. Wade, M. C. Foote, W. T. Elam, J. A. Hurowitz, S. Battel, D. E. Dawson, R. W. Denise, E. M. Ek, M. S. Gilbert, M. E. King, C. C. Liebe, T. Parker, D. A. K. Pedersen, D. P. Randall, R. F. Sharrow, M. E. Sondheim, G. Allen, K. Arnett, M. H. Au, C. Basset, M. Benn, J. C. Bousman, D. Braun, R. J. Calvet, B. Clark, L. Cinquini, S. Conaby, H. A. Conley, S. Davidoff, J. Delaney, T. Denver, E. Diaz, G. B. Doran, J. Ervin, M. Evans, D. O. Flannery, N. Gao, J. Gross, J. Grotzinger, B. Hannah, J. T. Harris, C. M. Harris, Y. He, C. M. Heirwegh, C. Hernandez, E. Hertzberg, R. P. Hodyss, J. R. Holden, C. Hummel, M. A. Jadusingh, J. L. Jørgensen, J. H. Kawamura, A. Kitiyakara, K. Kozaczek, J. L. Lambert, P. R. Lawson, Y. Liu, T. S. Luchik, K. M. Macneal, S. N. Madsen, S. M. McLennan, P. McNally, P. L. Meras, R. E. Muller, J. Napoli, B. J. Naylor, P. Nemere, I. Ponomarev, R. M. Perez, N. Pootrakul, R. A. Romero, R. Rosas, J. Sachs, R. T. Schaefer, M. E. Schein, T. P. Setterfield, V. Singh, E. Song, M. M. Soria, P. C. Stek, N. R. Tallarida, D. R. Thompson, M. M. Tice, L. Timmermann, V. Torossian, A. Treiman, S. Tsai, K. Uckert, J. Villalvazo, M. Wang, D. W. Wilson, S. C. Worel, P. Zamani, M. Zappe, F. Zhong, R. Zimmerman, PIXL: Planetary instrument for x-ray lithochemistry. *Space Sci. Rev.* **216**, 134 (2020).
12. L. Mandon, C. Quantin-Nataf, P. Thollot, N. Mangold, L. Lozac'h, G. Dromart, P. Beck, E. Dehouck, S. Breton, C. Millot, M. Volat, Refining the age, emplacement and alteration scenarios of the olivine-rich unit in the Nili Fossae region, Mars. *Icarus* **336**, 113436 (2020).
13. C. I. Fassett, J. W. Head, The timing of martian valley network activity: Constraints from buffered crater counting. *Icarus* **195**, 61–89 (2008).
14. T. A. Goudge, D. Mohrig, B. T. Cardenas, C. M. Hughes, C. I. Fassett, Stratigraphy and paleohydrology of delta channel deposits, Jezero crater, Mars. *Icarus* **301**, 58–75 (2018).
15. N. Mangold, S. Gupta, O. Gasnault, G. Dromart, J. D. Tarnas, S. F. Sholes, B. Horgan, C. Quantin-Nataf, A. J. Brown, S. le Mouélic, R. A. Yingst, J. F. Bell, O. Beyssac, T. Bosak, F. Calef III, B. L. Ehlmann, K. A. Farley, J. P. Grotzinger, K. Hickman-Lewis, S. Holm-Alwmark, L. C. Kah, J. Martinez-Frias, S. McLennan, S. Maurice, J. I. Nuñez, A. M. Ollila, P. Pilleri, J. W. Rice Jr., M. Rice, J. I. Simon, D. L. Shuster, K. M. Stack, V. Z. Sun, A. H. Treiman, B. P. Weiss, R. C. Wiens, A. J. Williams, N. R. Williams, K. H. Williford, Perseverance rover reveals an ancient delta-lake system and flood deposits at Jezero crater, Mars. *Science* **374**, 711–717 (2021).
16. N. Mangold, G. Dromart, V. Ansan, F. Salese, M. G. Kleinhans, M. Massé, C. Quantin-Nataf, K. M. Stack, Fluvial regimes, morphometry, and age of Jezero crater paleolake inlet valleys and their exobiological significance for the 2020 rover mission landing site. *Astrobiology* **20**, 994–1013 (2020).
17. K. A. Farley, K. M. Stack, D. L. Shuster, B. H. N. Horgan, J. A. Hurowitz, J. D. Tarnas, J. I. Simon, V. Z. Sun, E. L. Scheller, K. R. Moore, S. M. McLennan, P. M. Vasconcelos, R. C. Wiens, A. H. Treiman, L. E. Mayhew, O. Beyssac, T. V. Kizovski, N. J. Tosca, K. H. Williford, L. S. Crumpler, L. W. Beegle, J. F. Bell III, B. L. Ehlmann, Y. Liu, J. N. Maki, M. E. Schmidt, A. C. Allwood, H. E. F. Amundsen, R. Bhartia, T. Bosak, A. J. Brown, B. C. Clark, A. Cousin, O. Forni, T. S. J. Gabriel, Y. Goreva, S. Gupta, S.-E. Hamran, C. D. K. Herd, K. Hickman-Lewis, J. R. Johnson, L. C. Kah, P. B. Kelemen, K. B. Kinch, L. Mandon, N. Mangold, C. Quantin-Nataf, M. S. Rice, P. S. Russell, S. Sharma, S. Siljeström, A. Steele, R. Sullivan, M. Wadhwa, B. P. Weiss, A. J. Williams, B. V. Wogsland, P. A. Willis, T. A. Acosta-Maeda, P. Beck, K. Benzerara, S. Bernard, A. S. Burton, E. L. Cardarelli, B. Chide, E. Clavé, E. A. Cloutis, B. A. Cohen, A. D. Czaja, V. Debaille, E. Dehouck, A. G. Fairén, D. T. Flannery, S. Z. Fleron, T. Fouchet, J. Frydenvang, B. J. Garczynski, E. F. Gibbons, E. M. Hausrath, A. G. Hayes, J. Henneke, J. L. Jørgensen, E. M. Kelly, J. Lasue, S. Le Mouélic, J. M. Madariaga, S. Maurice, M. Merusi, P.-Y. Meslin, S. M. Milkovich, C. C. Million, R. C. Moeller, J. I. Núñez, A. M. Ollila, G. Paar, D. A. Paige, D. A. K. Pedersen, P. Pilleri, C. Pilorget, P. C. Pinet, J. W. Rice Jr., C. Royer, V. Sautter, M. Schulte, M. A. Sephton, S. K. Sharma, S. F. Sholes, N. Spanovich, M. St. Clair, C. D. Tate, K. Uckert, S. J. Van Bommel, A. G. Yanchilina, M.-P. Zorzano, Aqueously altered igneous rocks sampled on the floor of Jezero crater, Mars. *Science* **377**, eabo2196 (2022).
18. M. S. Bramble, J. F. Mustard, M. R. Salvatore, The geological history of Northeast Syrtis Major, Mars. *Icarus* **293**, 66–93 (2017).
19. B. L. Ehlmann, J. F. Mustard, An in-situ record of major environmental transitions on early Mars at Northeast Syrtis Major. *Geophys. Res. Lett.* **39**, L11202 (2012).
20. J. L. Bishop, D. Tirsch, L. L. Tornabene, R. Jaumann, A. S. McEwen, P. C. McGuire, A. Ody, F. Poulet, R. N. Clark, M. Parente, N. K. McKeown, J. F. Mustard, S. L. Murchie, J. Voigt,

Z. Aydin, M. Bamberg, A. Petau, G. Michael, F. P. Seelos, C. D. Hash, G. A. Swayze, G. Neukum, Mineralogy and morphology of geologic units at Libya Montes, Mars: Ancient aqueously derived outcrops, mafic flows, fluvial features, and impacts. *J. Geophys. Res.* **118**, 487–513 (2013).
21. C. H. Kremer, J. F. Mustard, M. S. Bramble, A widespread olivine-rich ash deposit on Mars. *Geology* **47**, 677–681 (2019).
22. T. M. Hoefen, R. N. Clark, J. L. Bandfield, M. D. Smith, J. C. Pearl, P. R. Christensen, Discovery of olivine in the Nili Fossae region of Mars. *Science* **302**, 627–630 (2003).
23. V. E. Hamilton, P. R. Christensen, Evidence for extensive, olivine-rich bedrock on Mars. *Geology* **33**, 433–436 (2005).
24. A. D. Rogers, N. H. Warner, M. P. Golombek, J. W. Head III, J. C. Cowart, Areally extensive surface bedrock exposures on Mars: Many are clastic rocks, not lavas. *Geophys. Res. Lett.* **45**, 1767–1777 (2018).
25. Y. Liu, M. M. Tice, M. E. Schmidt, A. H. Treiman, T. V. Kizovski, J. A. Hurowitz, A. C. Allwood, J. Henneke, D. A. K. Pedersen, S. J. Van Bommel, M. W. M. Jones, A. L. Knight, B. J. Orenstein, B. C. Clark, W. T. Elam, C. M. Heirwegh, T. Barber, L. W. Beegle, K. Benzerara, S. Bernard, O. Beyssac, T. Bosak, A. J. Brown, E. L. Cardarelli, D. C. Catling, J. R. Christian, E. A. Cloutis, B. A. Cohen, S. Davidoff, A. G. Fairén, K. A. Farley, D. T. Flannery, A. Galvin, J. P. Grotzinger, S. Gupta, J. Hall, C. D. K. Herd, K. Hickman-Lewis, R. P. Hodyss, B. H. N. Horgan, J. R. Johnson, J. L. Jørgensen, L. C. Kah, J. N. Maki, L. Mandon, N. Mangold, F. M. McCubbin, S. M. McLennan, K. Moore, M. Nachon, P. Nemere, L. D. Nothdurft, J. I. Núñez, L. O'Neil, C. M. Quantin-Nataf, V. Sautter, D. L. Shuster, K. L. Siebach, J. I. Simon, K. P. Sinclair, K. M. Stack, A. Steele, J. D. Tarnas, N. J. Tosca, K. Uckert, A. Udry, L. A. Wade, B. P. Weiss, R. C. Wiens, K. H. Williford, M.-P. Zorzano, An olivine cumulate outcrop on the floor of Jezero crater, Mars. *Science* **377**, 1513–1519 (2022).
26. K. A. Farley, P. Martin, P. D. Archer Jr., S. K. Atreya, P. G. Conrad, J. L. Eigenbrode, A. G. Fairén, H. B. Franz, C. Freissinet, D. P. Glavin, P. R. Mahaffy, C. Malespin, D. W. Ming, R. Navarro-Gonzalez, B. Sutter, Light and variable $^{37}Cl/^{35}Cl$ ratios in rocks from Gale Crater, Mars: Possible signature of perchlorate. *Earth Planet. Sci. Lett.* **438**, 14–24 (2016).
27. A. J. Brown, S. J. Hook, A. M. Baldridge, J. K. Crowley, N. T. Bridges, B. J. Thomson, G. M. Marion, C. R. de Souza Filho, J. L. Bishop, Hydrothermal formation of Clay-Carbonate alteration assemblages in the Nili Fossae region of Mars. *Earth Planet. Sci. Lett.* **297**, 174–182 (2010).
28. A. J. Brown, C. E. Viviano, T. A. Goudge, Olivine-carbonate mineralogy of the Jezero crater region. *J. Geophys. Res.* **125**, e2019JE006011 (2020).
29. E. L. Scheller, C. Swindle, J. Grotzinger, H. Barnhart, S. Bhattacharjee, B. L. Ehlmann, K. Farley, W. W. Fischer, Formation of magnesium carbonates on Earth and implications for Mars. *J. Geophys. Res.* **126**, e2021JE006828 (2021).
30. C. E. Viviano, J. E. Moersch, H. Y. McSween, Implications for early hydrothermal environments on Mars through the spectral evidence for carbonation and chloritization reactions in the Nili Fossae region. *J. Geophys. Res.* **118**, 1858–1872 (2013).
31. A. M. Zastrow, T. D. Glotch, Distinct carbonate lithologies in Jezero crater, Mars. *Geophys. Res. Lett.* **48**, e2020GL092365 (2021).
32. R. C. Moeller, L. Jandura, K. Rosette, M. Robinson, J. Samuels, M. Silverman, K. Brown, E. Duffy, A. Yazzie, E. Jens, I. Brockie, L. White, Y. Goreva, T. Zorn, A. Okon, J. Lin, M. Frost, C. Collins, J. B. Williams, A. Steltzner, F. Chen, J. Biesiadecki, The Sampling and Caching Subsystem (SCS) for the scientific exploration of Jezero crater by the Mars 2020 Perseverance Rover. *Space Sci. Rev.* **217**, 5 (2021).
33. R. C. Wiens, A. Udry, O. Beyssac, C. Quantin-Nataf, N. Mangold, A. Cousin, L. Mandon, T. Bosak, O. Forni, S. M. McLennan, V. Sautter, A. Brown, K. Benzerara, J. R. Johnson, L. Mayhew, S. Maurice, R. B. Anderson, S. M. Clegg, L. Crumpler, T. S. J. Gabriel, P. Gasda, J. Hall, B. H. N. Horgan, L. Kah, C. Legett IV, J. M. Madariaga, P.-Y. Meslin, A. M. Ollila, F. Poulet, C. Royer, S. K. Sharma, S. Siljeström, J. I. Simon, T. E. Acosta-Maeda, C. Alvarez-Llamas, S. M. Angel, G. Arana, P. Beck, S. Bernard, T. Bertrand, B. Bousquet, K. Castro, B. Chide, E. Clavé, E. Cloutis, S. Connell, E. Dehouck, G. Dromart, W. Fischer, T. Fouchet, R. Francis, J. Frydenvang, O. Gasnault, E. Gibbons, S. Gupta, E. M. Hausrath, X. Jacob, H. Kalucha, E. Kelly, E. Knutsen, N. Lanza, J. Laserna, J. Lasue, S. L. Mouélic, R. Leveille, G. L. Reyes, R. Lorenz, J. A. Manrique, J. Martinez-Frias, T. M. Connochie, N. Melikechi, D. Mimoun, F. Montmessin, J. Moros, N. Murdoch, P. Pilleri, C. Pilorget, P. Pinet, W. Rapin, F. Rull, S. Schröder, D. L. Shuster, R. J. Smith, A. E. Stott, J. Tarnas, N. Turenne, M. Veneranda, D. S. Vogt, B. P. Weiss, P. Willis, K. M. Stack, K. H. Williford, K. A. Farley; SuperCam Team, Compositionally and density stratified igneous terrain in Jezero crater, Mars. *Sci. Adv.* **8**, eabo3399 (2022).
34. C. S. Romanek, C. Jiménez-López, A. R. Navarro, M. Sánchez-Román, N. Sahai, M. Coleman, Inorganic synthesis of Fe–Ca–Mg carbonates at low temperature. *Geochim. Cosmochim. Acta* **73**, 5361–5376 (2009).
35. E. Scheller *et al.*, Aqueous alteration processes and implications for organic geochemistry in Jezero crater, Mars.*Science*, (under consideration).
36. S. J. Chipera, D. T. Vaniman, Experimental stability of magnesium sulfate hydrates that may be present on Mars. *Geochim. Cosmochim. Acta* **71**, 241–250 (2007).
37. G. M. Hansford, Back-reflection energy-dispersive x-ray diffraction: A novel diffraction technique with almost complete insensitivity to sample morphology. *J. Appl. Cryst.* **44**, 514–525 (2011).
38. G. M. Hansford, X-ray diffraction without sample preparation: Proof-of-principle experiments. *Nucl. Instrum. Methods Phys. Res. Sec. A* **728**, 102–106 (2013).
39. W. Nikonow, D. Rammlmair, Risk and benefit of diffraction in energy dispersive x-ray fluorescence mapping. *Spectrochim. Acta B* **125**, 120–126 (2016).
40. J. Delvigne, E. Bisdom, J. Sleeman, G. Stoops, Olivines, their pseudomorphs and secondary products. *Pedologie* **29**, 247–309 (1979).
41. E. M. Hausrath, S. L. Brantley, Basalt and olivine dissolution under cold, salty, and acidic conditions: What can we learn about recent aqueous weathering on Mars? *J. Geophys. Res.* **115**, E12001 (2010).
42. C. Boschi, A. Dini, L. Dallai, G. Ruggieri, G. Gianelli, Enhanced CO_2-mineral sequestration by cyclic hydraulic fracturing and Si-rich fluid infiltration into serpentinites at Malentrata (Tuscany, Italy). *Chem. Geol.* **265**, 209–226 (2009).
43. D. Daval, O. Sissmann, N. Menguy, G. D. Saldi, F. Guyot, I. Martinez, J. Corvisier, B. Garcia, I. Machouk, K. G. Knauss, R. Hellmann, Influence of amorphous silica layer formation on the dissolution rate of olivine at 90°C and elevated pCO_2. *Chem. Geol.* **284**, 193–209 (2011).
44. J. M. Matter, P. B. Kelemen, Permanent storage of carbon dioxide in geological reservoirs by mineral carbonation. *Nat. Geosci.* **2**, 837–841 (2009).
45. W. Xiong, R. K. Wells, A. H. Menefee, P. Skemer, B. R. Ellis, D. E. Giammar, CO_2 mineral trapping in fractured basalt. *Int. J. Greenh. Gas Control* **66**, 204–217 (2017).
46. N. C. Johnson, B. Thomas, K. Maher, R. J. Rosenbauer, D. Bird, G. E. Brown Jr., Olivine dissolution and carbonation under conditions relevant for in situ carbon storage. *Chem. Geol.* **373**, 93–105 (2014).
47. J. H. Kwak, J. Z. Hu, R. V. F. Turcu, K. M. Rosso, E. S. Ilton, C. Wang, J. A. Sears, M. H. Engelhard, A. R. Felmy, D. W. Hoyt, The role of H_2O in the carbonation of forsterite in supercritical CO_2. *Int. J. Greenh. Gas Control* **5**, 1081–1092 (2011).
48. K. Maher, N. C. Johnson, A. Jackson, L. N. Lammers, A. B. Torchinsky, K. L. Weaver, D. K. Bird, G. E. Brown Jr., A spatially resolved surface kinetic model for forsterite dissolution. *Geochim. Cosmochim. Acta* **174**, 313–334 (2016).
49. L. E. Mayhew, E. T. Ellison, H. M. Miller, P. B. Kelemen, A. S. Templeton, Iron transformations during low temperature alteration of variably serpentinized rocks from the Samail ophiolite, Oman. *Geochim. Cosmochim. Acta* **222**, 704–728 (2018).
50. A. Neubeck, N. T. Duc, H. Hellevang, C. Oze, D. Bastviken, Z. Bacsik, N. G. Holm, Olivine alteration and H2 production in carbonate-rich, low temperature aqueous environments. *Planet. Space Sci.* **96**, 51–61 (2014).
51. M. C. Johnson, M. J. Rutherford, P. C. Hess, Chassigny petrogenesis: Melt compositions, intensive parameters and water contents of Martian magmas. *Geochim. Cosmochim. Acta* **55**, 349–366 (1991).
52. L. Chai, A. Navrotsky, Synthesis, characterization, and enthalpy of mixing of the (Fe,Mg)C0 3 solid solution. *Geochim. Cosmochim. Acta* **60**, 4377–4383 (1996).
53. A. C. Lasaga, in *Kinetic Theory in the Earth Sciences*, A. C. Lasaga, Ed. (Princeton University Press, 2014), pp. 497-580. doi:10.1515/9781400864874.497.
54. C. Neal, G. Stanger, Past and present serpentinization of ultramafic rocks: An example from the Semail ophiolite nappe of northern Oman, in *The Chemistry of Weathering*, J. I. Drever, Ed. (Springer, 1985), pp. 249–275.
55. F. Klein, W. Bach, T. M. McCollom, Compositional controls on hydrogen generation during serpentinization of ultramafic rocks. *Lithos* **178**, 55–69 (2013).
56. H.-T. Lin, J. P. Cowen, E. J. Olson, M. D. Lilley, S. P. Jungbluth, S. T. Wilson, M. S. Rappé, Dissolved hydrogen and methane in the oceanic basaltic biosphere. *Earth Planet. Sci. Lett.* **405**, 62–73 (2014).
57. A. Steele, L. G. Benning, R. Wirth, A. Schreiber, T. Araki, F. M. McCubbin, M. D. Fries, L. R. Nittler, J. Wang, L. J. Hallis, P. G. Conrad, C. Conley, S. Vitale, A. C. O'Brien, V. Riggi, K. Rogers, Organic synthesis associated with serpentinization and carbonation on early Mars. *Science* **375**, 172–177 (2022).
58. C. S. Cockell, Life in the lithosphere, kinetics and the prospects for life elsewhere. *Philos. Trans. R. Soc. A Math. Phys. Eng. Sci.* **369**, 516–537 (2011).
59. F. Westall, F. Foucher, N. Bost, M. Bertrand, D. Loizeau, J. L. Vago, G. Kminek, F. Gaboyer, K. A. Campbell, J.-G. Bréhéret, P. Gautret, C. S. Cockell, Biosignatures on Mars: What, where, and how? Implications for the search for martian life. *Astrobiology* **15**, 998–1029 (2015).
60. R. M. Cesur, I. M. Ansari, F. Chen, B. C. Clark, M. A. Schneegurt, Bacterial growth in brines formed by the deliquescence of salts relevant to cold arid worlds. *Astrobiology* **22**, 104–115 (2022).
61. M. M. Walsh, Evaluation of early Archean volcaniclastic and volcanic flow rocks as possible sites for carbonaceous fossil microbes. *Astrobiology* **4**, 429–437 (2004).
62. A. C. Allwood, I. W. Burch, J. M. Rouchy, M. Coleman, Morphological biosignatures in gypsum: Diverse formation processes of Messinian (~6.0 Ma) gypsum stromatolites. *Astrobiology* **13**, 870–886 (2013).
63. L. E. Hays, H. V. Graham, D. J. Des Marais, E. M. Hausrath, B. Horgan, T. M. McCollom, M. N. Parenteau, S. L. Potter-McIntyre, A. J. Williams, K. L. Lynch, Biosignature preservation and detection in Mars analog environments. *Astrobiology* **17**, 363–400 (2017).
64. S. McMahon, T. Bosak, J. P. Grotzinger, R. E. Milliken, R. E. Summons, M. Daye, S. A. Newman, A. Fraeman, K. H. Williford, D. E. G. Briggs, A field guide to finding fossils on Mars. *J. Geophys. Res.* **123**, 1012–1040 (2018).

65. A. Steele, L. G. Benning, R. Wirth, S. Siljeström, M. D. Fries, E. Hauri, P. G. Conrad, K. Rogers, J. Eigenbrode, A. Schreiber, A. Needham, J. H. Wang, F. M. McCubbin, D. Kilcoyne, J. D. Rodriguez Blanco, Organic synthesis on Mars by electrochemical reduction of CO_2. *Sci. Adv.* **4**, eaat5118 (2018).
66. H. Franz, P. R. Mahaffy, C. R. Webster, G. J. Flesch, E. Raaen, C. Freissinet, S. K. Atreya, C. H. House, A. C. McAdam, C. A. Knudson, P. D. Archer Jr., J. C. Stern, A. Steele, B. Sutter, J. L. Eigenbrode, D. P. Glavin, J. M. T. Lewis, C. A. Malespin, M. Millan, D. W. Ming, R. Navarro-González, R. E. Summons, Indigenous and exogenous organics and surface–atmosphere cycling inferred from carbon and oxygen isotopes at Gale crater. *Nat. Astron.* **4**, 526–532 (2020).
67. S. P. Kounaves, B. L. Carrier, G. D. O'Neil, S. T. Stroble, M. W. Claire, Evidence of martian perchlorate, chlorate, and nitrate in Mars meteorite EETA79001: Implications for oxidants and organics. *Icarus* **229**, 206–213 (2014).
68. M. H. Hecht, S. P. Kounaves, R. C. Quinn, S. J. West, S. M. M. Young, D. W. Ming, D. C. Catling, B. C. Clark, W. V. Boynton, J. Hoffman, L. P. DeFlores, K. Gospodinova, J. Kapit, P. H. Smith, Detection of perchlorate and the soluble chemistry of martian soil at the phoenix lander site. *Science* **325**, 64–67 (2009).
69. B. Sutter, A. C. McAdam, P. R. Mahaffy, D. W. Ming, K. S. Edgett, E. B. Rampe, J. L. Eigenbrode, H. B. Franz, C. Freissinet, J. P. Grotzinger, A. Steele, C. H. House, P. D. Archer, C. A. Malespin, R. Navarro-González, J. C. Stern, J. F. Bell, F. J. Calef, R. Gellert, D. P. Glavin, L. M. Thompson, A. S. Yen, Evolved gas analyses of sedimentary rocks and eolian sediment in Gale Crater, Mars: Results of the Curiosity rover's sample analysis at Mars instrument from Yellowknife Bay to the Namib Dune. *J. Geophys. Res.* **122**, 2574–2609 (2017).
70. A. H. Treiman, R. A. Barrett, J. L. Gooding, Preterrestrial aqueous alteration of the Lafayette (SNC) meteorite. *Meteoritics* **28**, 86–97 (1993).
71. K. Mitra, E. L. Moreland, J. G. Catalano, Capacity of chlorate to oxidize ferrous iron: Implications for iron oxide formation on Mars. *Minerals* **10**, 729 (2020).
72. D. Catling, M. W. Claire, K. J. Zahnle, R. C. Quinn, B. C. Clark, M. H. Hecht, S. Kounaves, Atmospheric origins of perchlorate on Mars and in the Atacama. *J. Geophys. Res.* **115**, E00E11 (2010).
73. M. L. Smith, M. W. Claire, D. C. Catling, K. J. Zahnle, The formation of sulfate, nitrate and perchlorate salts in the martian atmosphere. *Icarus* **231**, 51–64 (2014).
74. J. D. Toner, D. C. Catling, Chlorate brines on Mars: Implications for the occurrence of liquid water and deliquescence. *Earth Planet. Sci. Lett.* **497**, 161–168 (2018).
75. A. Zheng, A. Casari, *Feature Engineering for Machine Learning: Principles and Techniques for Data Scientists* (O'Reilly Media Inc., 2018).
76. S. R. Safavian, D. Landgrebe, A survey of decision tree classifier methodology. *IEEE Trans. Syst. Man Cybern.* **21**, 660–674 (1991).
77. P. Refaeilzadeh, L. Tang, H. Liu, Cross-validation, in *Encyclopedia of Database Systems* (Springer, 2009), vol. 5, pp. 532–538 .
78. D. Dragoi, A. Dragoi, Modeling of energy-dispersive x-ray diffraction for high-symmetry crystal orientation. *Acta Crystallogr. A* **75**, 63–70 (2019).
79. P. Coppens, in *International Tables for Crystallography, Volume B: Reciprocal Space*, U. Shmueli, Ed. (Springer, 2006), chap. 1.2, pp. 10–24.
80. D. A. K. Pedersen, C. C. Liebe, J. L. Jorgensen, Structured light system on Mars Rover robotic arm instrument. *IEEE Trans. Aerosp. Electron. Syst.* **55**, 1612–1623 (2019).

Acknowledgments: We are grateful to Mars 2020 team members who participated in tactical and strategic science operations. We acknowledge T. Wang (Central Analytical Research Facility, Queensland University of Technology) for assistance with theoretically modeling EDXRD. **Funding:** The work described in this paper was partially carried out at the Jet Propulsion Laboratory, California Institute of Technology, under a prime contract with the National Aeronautics and Space Administration (80NM0018D0004). M.M.T., J.A.H., A.C.A., S.D., A.P.W., K.R.M., B.C.C., S.M.M., A.S., A.J.B., Y.L., A.H.T., and L.O. were supported by NASA grant 80NM0018D0004 through J.P.L. S.J.V. and D.L.S. were supported by the NASA M2020 Participating Scientist Programs. M.E.S. and T.V.K. were supported by the Canadian Space Agency M2020 Participating Scientist grants. K.H.-L. was supported by a UK Space Agency Aurora Research Fellowship. A.G.F. was supported by the European Research Council CoG no. 818602. S.G. was supported by the U.K. Space Agency and Royal Society (SRF\R1\21000106). D.T.F. was supported by Australian Research Council grant DE210100205. D.A.K.P. and J.H. were supported by the National Space Institute, Technical University of Denmark. N.J.T. was supported by the Cambridge University. S.G. was supported by the Royal Society Leverhulme Trust Senior Research Fellowship (SRF\R1\21000106) and the U.K. Space Agency (grant numbers: ST/X002373/1 and ST/S001492/1). **Author contributions:** M.M.T. led the writing of the manuscript. M.M.T., J.A.H., A.C.A., M.W.M.J., B.J.O., S.D., A.P.W., D.A.K.P., J.H., N.J.T., K.R.M., B.C.C., S.M.M., D.T.F., A.S., A.J.B., M.P.Z., K.H.L., Y.L., and S.J.V. prepared the original draft with input from A.G.F., D.L.S., and S.G. All authors provided input to the manuscript through discussion, editing, or reviewing. M.M.T., J.A.H., A.C.A., M.W.M.J., B.J.O., D.A.K.P., J.H., N.J.T., K.R.M., B.C.C., D.T.F., Y.L., S.J.V., M.E.S., T.V.K., A.H.T., and L.O. contributed to the design, execution, and analysis of PIXL observations. All authors contributed to the selection and geologic interpretation of the rocks discussed here. M.M.T., M.W.M.J., B.J.O., S.D., A.P.W., D.A.K.P., J.H., and B.C.C. performed data processing and analysis. M.M.T., M.W.M.J., B.J.O., S.D., A.P.W., D.A.K.P., J.H., and B.C.C. prepared visualizations. Project management of the PIXL investigation was by A.C.A. and J.A.H. **Competing interests:** The authors declare that they have no competing interests. **Data and materials availability:** All data needed to evaluate the conclusions in the paper are present in the paper and/or the Supplementary Materials. PIXL images and data used in this paper are available on the Planetary Data System (PDS; doi:10.17189/1522645; https://pds.nasa.gov/ds-view/pds/viewBundle.jsp?identifier=urn%3Anasa%3Apds%3Amars2020_pixl&version=1.0).

Submitted 6 March 2022
Accepted 29 September 2022
Published 23 November 2022
10.1126/sciadv.abp9084